catalysts

MDPI

Review

Symmetry Design of Metal–Organic Frameworks for High-Performance Piezocatalysis: Fundamental Mechanisms and Multi-Scale Structural Regulation

Kailai Zhang [1,2,†], Ao Feng [1,2,†], Aoan Chen [1,2], Hang Chen [1,2], Shurui Xu [1,2,*], Guoyu Zhong [1,2,*] and Baizeng Fang [1,2,*]

[1] Innovation Catalysis Team, School of Chemical Engineering and Energy Technology, Dongguan University of Technology, Dongguan 523808, China; zhangkl1996@163.com (K.Z.); fengao514@163.com (A.F.); chenaoan1124@163.com (A.C.); chenhang@dgut.edu.cn (H.C.)

[2] Guangdong Provincial Key Laboratory of Multi-Energy Complementary Distributed Energy Systems, School of Chemical Engineering and Energy Technology, Dongguan University of Technology, Dongguan 523808, China

* Correspondence: xusr@dgut.edu.cn (S.X.); zhonggy@dgut.edu.cn (G.Z.); baizengfang@163.com (B.F.)

† These authors contributed equally to this work.

Abstract

Driven by the pursuit of carbon-neutral and distributed energy systems, extensive efforts have been devoted to harvesting ubiquitous low-grade ambient mechanical energy. Piezocatalysis offers a unique light-independent and electricity-free pathway that converts mechanical vibration into reactive radical species. Conventional inorganic ferroelectrics and piezoelectric polymers face severe limitations originating from rigid lattice configurations, insufficient surface active sites, and unmodulable electronic band structures. Benefiting from reticular chemistry, metal-organic frameworks (MOFs) emerge as versatile piezoactive candidates. Crystallographic inversion symmetry, which acts as the core determinant of intrinsic lattice dipoles and strain-activated charge screening behavior, can be precisely regulated at the molecular level. Most existing reviews classify MOFs piezocatalysts primarily by metal-node types. However, a systematic analytical framework centered on symmetry breaking to clarify structure-activity relationships is still lacking. This review establishes a multi-scale symmetry modulation paradigm focusing on crystal inversion-symmetry engineering. It comprehensively demonstrates three fundamentally piezocatalytic mechanisms and systematically highlights the unique piezoelectric structural superiority of tunable MOFs over traditional piezoelectric materials. This work elaborates a three-tier symmetry engineering strategy covering intrinsic lattice regulation, metal-mediated dipole amplification, and multicomponent heterostructure construction. It summarizes full-scale bottlenecks involving fundamental mechanisms, material design, and device integration. This review delivers symmetry-oriented structural principles and theoretical support for the efficient utilization of low-grade mechanical energy. Finally, it discusses the prospects of artificial intelligence-assisted high-throughput screening to advance the rational exploration of high-performance, symmetry-compliant piezocatalytic MOFs.

Keywords: metal–organic frameworks; piezocatalysis; crystal symmetry; structure–property relationship

Received: 18 August 2026
Revised: 15 September 2026
Accepted: 23 September 2026
Published: 24 September 2026

1. Introduction

Converting renewable-energy-driven chemical fuel production to tackle the global energy crisis and mitigate anthropogenic environmental contamination represents a critical research direction for environmentally benign catalytic technologies [1,2]. Proposed in 2010, piezocatalysis circumvents the cascaded mechanical-electric-chemical energy loss pathway [3]. Under tensile or compressive strain, lattice polarization charges directly generate redox-active intermediates, enabling one-step conversion of vibrational energy into chemical driving force and igniting a decade-long global research surge on piezoelectric functional materials.

The physical foundation of piezocatalysis originates from the piezoelectric effect. Upon mechanical deformation, non-centrosymmetric crystalline lattices realize the spatial separation of cation-anion charge centers to form intrinsic built-in electrostatic fields that dissociate strain-derived electron–hole pairs [4–10]. Three complementary interpretative theories have been established to rationalize diverse piezocatalytic phenomena. Strain-triggered band bending tends to prevail under high-power ultrasonic excitation, whereas dynamic space-charge screening frequently plays a major role under low-grade weak-vibration conditions. Maxwell displacement current theory delivers a unified description valid for both semiconducting and insulating piezo-materials [11,12].

Two distinct sets of fundamental prerequisites govern piezocatalytic processes, depending on the dominant operating mechanism. For band-mediated piezocatalysis occurring in piezoelectric semiconductors, two indispensable conditions must be satisfied: non-centrosymmetric crystal space groups to sustain lattice dipoles, and semiconductor band edges thermodynamically aligned with the target redox potentials. By contrast, for piezocatalysis driven by displacement current or interfacial space-charge screening effects, which applies to both semiconducting and insulating piezoelectric materials, a non-centrosymmetric crystal lattice constitutes the core requirement, whereas well-defined semiconductor band alignment is not an essential prerequisite. State-of-the-art piezoelectric materials fall into two canonical families, both constrained by inherent structural drawbacks. Rigid inorganic piezo-crystals such as ZnO and $BaTiO_3$, feature dense stacking, low specific surface areas and fixed elemental compositions that block flexible band engineering [13,14]. PVDF-type polymers, despite superior mechanical pliability, suffer low dielectric constants that trigger ultrafast carrier recombination and drastically reduce catalytic throughput [15–20]. These intrinsic limitations degrade their performance under natural weak vibrational environments.

MOFs, crystalline hybrid solids assembled via reticular coordination chemistry from inorganic SBUs and organic linkers, possess atomically tunable architectures, permanent interconnected pores, and continuously adjustable band structures [21–35]. Their most distinctive advantage over conventional piezo-substrates lies in the artificial modulation of crystallographic inversion symmetry, a core structural parameter determining lattice dipole magnitude and surface shielding charge density.

The evolutionary timeline of MOFs piezocatalysis unfolds across three distinct research epochs. The exploratory phase launched in 2008, when SHG characterizations of chiral imazethapyr MOFs first validated non-centrosymmetric ferroelectricity within coordination lattices [36]. In 2011, Lin's group demonstrated that directional metal–ligand coordination bonds could construct MOFs with superior SHG performance to commercial $LiNbO_3$ single crystals [37]. In 2019, Sun and co-workers demonstrated the favorable ferroelectric behaviors of UiO-66-type MOF materials [38]. Relative to their non-functionalized counterparts, UiO-66 derivatives decorated with -NH_2, -OH, and -COOH moieties exhibit substantially improved piezoelectric responses, rendering them competent piezocatalytic candidates. Notably, the piezocatalytic degradation of dye wastewater by NH_2-UiO-66 was

initially documented in 2020 [39]. This milestone discovery has substantially propelled the development of NH_2-UiO-66-based piezocatalysis. In 2021, Zhang et al. reported the pioneering investigation employing Zr-based UiO-66-NH_2 and Hf-substituted UiO-66-NH_2 toward the piezocatalytic hydrogen evolution reaction [40].

Benefiting from intrinsic merits, including well-defined structural periodicity, robust framework skeletons, abundant pore channels, large specific surface areas, and outstanding chemical resistance, MOFs platforms stand out as compelling contenders for piezocatalytic energy-conversion scenarios [41–45]. Driven by these unique advantages, accumulating research efforts have continuously advanced this fast-developing discipline. Under such circumstances, summarizing the state-of-the-art progress and outlining future research perspectives becomes both imperative and timely.

Several dedicated review articles have recapitulated the progress of MOFs-based piezocatalysis [2,41]. Both reviews comprehensively address the merits of MOFs, such as high piezoelectric/ferroelectric responses, structural tunability, large surface areas, and chemical stability, and both survey enhancement strategies, including morphological control, metal doping, defect engineering, and heterojunction construction [2,41]. Nevertheless, these valuable summaries predominantly classify MOFs piezocatalysts by metal-node species or prototype MOF families, and their mechanistic discussion largely relies on the piezoelectric effect and energy-band theory without establishing a unified crystallographic perspective.

Despite these contributions, existing reviews dedicated to MOFs still lack an analytical paradigm centered on crystallographic symmetry, which is the fundamental determinant of strain-induced polarization. Various performance-boosting strategies are discussed in a discrete, category-by-category manner, without establishing causal links between modification routes and the symmetry variation in MOFs lattices [2,41]. Multi-scale symmetry regulation pathways are not hierarchically organized, and a systematic comparative assessment of the three complementary piezocatalytic polarization theories remains absent. To fill this gap, the present review adopts a symmetry-breaking-centered framework that departs from the conventional classification driven by metal nodes or applications. We sort diverse modification strategies according to their capacity to alter lattice centrosymmetry, comparatively demonstrate the three core piezocatalytic polarization mechanisms, and construct a three-tier, multi-level symmetry modulation hierarchy spanning atomic lattice tuning, dipole amplification mediated by metal clusters, and multi-component interfacial composite engineering. Beyond summarizing experimental cases and application advances, we further propose performance evaluation metrics oriented toward symmetry engineering and analyze critical bottlenecks from the perspective of operando symmetry characterization and rational screening of symmetry-tunable MOFs piezocatalysts (Figure 1).

2. Fundamental Piezocatalytic Polarization Mechanisms

Piezocatalysis relies solely on ambient mechanical vibration to generate reactive charge carriers, the physical origin of which stems from the lattice polarization of non-centrosymmetric piezoelectric semiconductors. Three mutually complementary theoretical frameworks have been developed to interpret diverse piezocatalytic behaviors.

2.1. Strain-Triggered Band Bending Theory

Analogous to the carrier excitation principle in photocatalysis, periodic mechanical loading induces an intrinsic piezoelectric built-in electric field, which remodels the band alignment of semiconductors. Under sufficiently intense ultrasonic strain, both the conduction band and valence band become tilted to meet the thermodynamic requirements for water splitting and organic oxidation. The holes accumulating at the material surface participate in oxidation reactions, whereas electrons in the conduction band drive reduction processes.

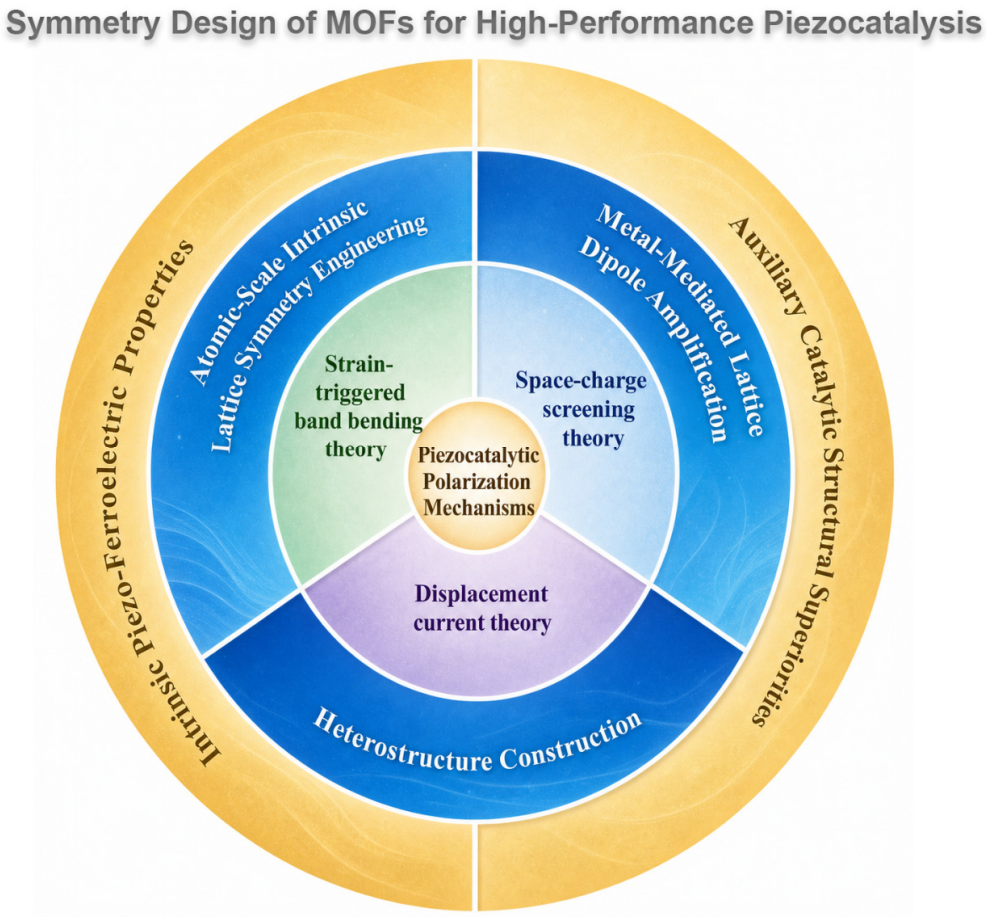

Figure 1. Graphic illustrating the multi-scale symmetry modulation framework for MOFs piezocatalysis.

This strain-triggered band-bending mechanism can be illustrated by the piezocatalytic system of $BiFeO_3$ nanosheets (Figure 2) [46]. As shown in Figure 2a, $BiFeO_3$ adopts a non-centrosymmetric crystal structure, which serves as the structural prerequisite for piezoelectricity. Upon mechanical vibration, lattice deformation occurs and generates bound polarization charges on the material surface (Figure 2b). The surface-bound positive charges oxidize sulfite to sulfate, while the negative charges drive the reduction of protons to produce H_2. Under static conditions without mechanical excitation (Figure 2c), the conduction band of $BiFeO_3$ nanosheets lies at a more positive potential relative to the H^+/H_2 redox level, failing to meet the thermodynamic requirement for hydrogen evolution. However, the piezoelectric polarization triggered by mechanical vibration creates an internal electric field within the material and induces band tilting (Figure 2d). The tilted band shifts the conduction band edge to a potential more negative than the H^+/H_2 level, satisfying the thermodynamic requirement for hydrogen production. Meanwhile, the piezoelectric built-in field spatially separates charge carriers: electrons migrate to the conduction band for H^+ reduction, and holes move to the valence band to oxidize sulfite, thereby enabling piezocatalytic hydrogen evolution.

2.2. Space-Charge Screening Theory

This framework centers on transient piezopotential oscillation and real-time surface charge compensation. Unlike static band bending induced by constant large strain, natural low-grade vibration (5–50 Hz) produces limited piezopotential fluctuation amplitude. Dissociated ions from aqueous media (H^+, OH^-), lattice oxygen vacancies, and other charged defects act as external/internal screening charges, continuously adsorbing on catalyst surfaces to counteract lattice-bound polarization charges.

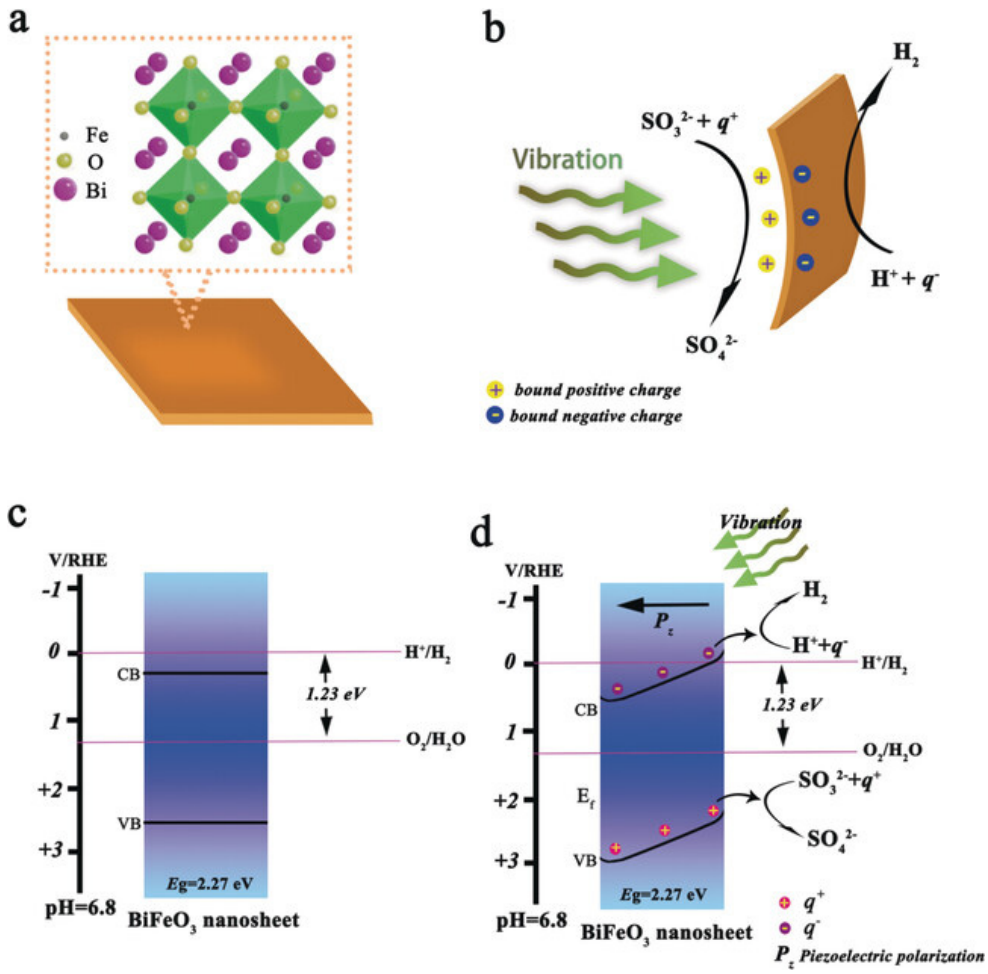

Figure 2. Schematic illustration of the piezocatalysis mechanism and tilting of energy bands. (**a**) Atomic structure of $BiFeO_3$. (**b**) The generation of piezoelectric surface charges under mechanical vibration and their participation in the piezocatalytic hydrogen evolution reaction. (**c**) Energy band diagram without mechanical vibration. (**d**) Tilting of energy bands under the strong piezoelectric field induced by mechanical vibration and the accompanying redox reactions. (Reprinted with permission from Ref. [46]. Copyright 2019, Wiley-VCH).

A terminological distinction is emphasized herein to separate two mechanically distinct excitation regimes. Low-grade mechanical vibration refers to ambient mechanical inputs within the 5–50 Hz frequency range without acoustic cavitation, typically with input power below 1 W, such as machinery oscillation, water-flow agitation, or human micromotion. In contrast, high-power ultrasonic excitation corresponds to 20–100 kHz acoustic irradiation, where cavitation-bubble implosion can generate transient local pressures up to 10^8 Pa. The two regimes produce significantly different strain rates, piezopotential amplitudes, and side-reaction contributions from sonochemistry and local thermal spikes. Importantly, piezocatalytic performance metrics acquired under high-intensity ultrasonic conditions cannot be directly extrapolated to low-grade ambient vibration scenarios, as the dominant mechanistic pathways may change with strain magnitude and loading frequency. Most reported experimental results for MOF piezocatalysis are collected under ultrasonic cavitation-dominated conditions.

Ultrasonic cavitation provides mechanical input for piezocatalysis (Figure 3) [47]. Periodic acoustic pressure cycles induce cavitation-bubble nucleation, growth, and catastrophic implosion, producing transient pressure reaching 10^8 Pa (Figure 3a,b). These shock stresses deform ferroelectric $BaTiO_3$ lattices and evoke dynamic oscillation of spontaneous polarization (Figure 3c). Along with polarization switching, surface positive and negative

charge densities at the solid-electrolyte interface are continuously modulated under constant total free-energy constraints. The dynamically accumulated negative surface charges enable CO_2-to-CO conversion, while positive holes oxidize water to yield·OH radicals. Cyclic lattice distortion triggered by cavitation-bubble implosion thus sustains continuous piezocatalytic redox processes.

This charge-screening-dominated picture is equally transferable to symmetry-engineered MOFs piezocatalysts, despite their absence of long-range ferroelectric domains analogous to $BaTiO_3$. In defective or heterometallic MOFs systems, local built-in potentials originate from distorted metal-cluster coordination rather than macroscopic spontaneous polarization. Under low-intensity mechanical perturbation, externally adsorbed electrolyte ions and mobile intrinsic defect charges rapidly screen those locally separated bound charges within MOFs secondary building units. Consequently, only a small fraction of unscreened residual charges survives to drive interfacial redox turnover, explaining the generally poor piezocatalytic performance of MOFs under mild ambient vibration. By contrast, high-amplitude shock pressure delivered by ultrasonic cavitation induces fast, large-magnitude local-potential oscillation. The rapid rate of piezopotential fluctuation outpaces the time scale of charge-screening relaxation, preserving sufficient uncompensated surface charges at MOFs active sites (metal nodes, single-atom centers, or defect sites) to sustain CO_2 reduction, H_2 evolution, or organic degradation.

2.3. Displacement Current Theory

Derived from Maxwell's equations, displacement current theory complements the two foregoing frameworks and unifies piezocatalytic charge generation in both semiconducting and insulating piezoelectric systems [48]. Periodic mechanical deformation rearranges lattice dipole moments, generating time-varying polarization fields that produce equivalent displacement current, the fundamental driving force for interfacial electron migration. No directional free conduction current forms inside the material; instead, time-dependent displacement current transfers charge carriers toward surface active sites to trigger catalysis.

For symmetry-modified MOF piezocatalysts, displacement-current-driven processes possess unique material-specific features distinct from rigid inorganic piezocrystals. Inorganic ferroelectrics mainly rely on the rotation or distortion of rigid inorganic polyhedra to alter macroscopic lattice dipoles. MOFs, by contrast, contain highly flexible organic linkers. Beyond the distortion of metal-node coordination polyhedra, cyclic mechanical stress can induce reversible torsion, bending, and swinging of these organic ligands and further modulate the magnitude of local dipole moments within the framework. Such linker-originated dipole fluctuations constitute an extra source of time-varying polarization that contributes to the overall displacement-current output, whether the MOFs behave as a semiconductor or an insulator. Unfortunately, most existing displacement-current theoretical models are built for dense, rigid inorganic lattices and do not incorporate the large-amplitude torsional degrees of freedom of organic link.

It should be noted that assigning the dominant piezocatalytic mechanism from experimental observations is far from straightforward, and common characterization techniques each have their own scope and limitations. It is important to clarify what each characterization technique can and cannot establish. EPR spectroscopy can provide direct evidence for the generation of reactive radical species, yet the presence of such radicals does not by itself prove a band-bending mechanism. FTIR spectroscopy can identify adsorbed intermediates analogous to those observed in electrocatalysis, but such intermediate identification does not uniquely establish space-charge screening. A transient current measured in a piezoelectric nanogenerator configuration can reflect the overall charge output, yet it cannot automatically isolate the Maxwell displacement-current contribution from conductive, capacitive, interfa-

cial, or triboelectric contributions. Consequently, rigorous mechanistic assignment cannot rely on any single measurement. It requires well-designed control experiments, calibrated strain-potential measurements, frequency-dependent responses, and multi-modal operando spectroscopy, which remain open topics for future dedicated studies.

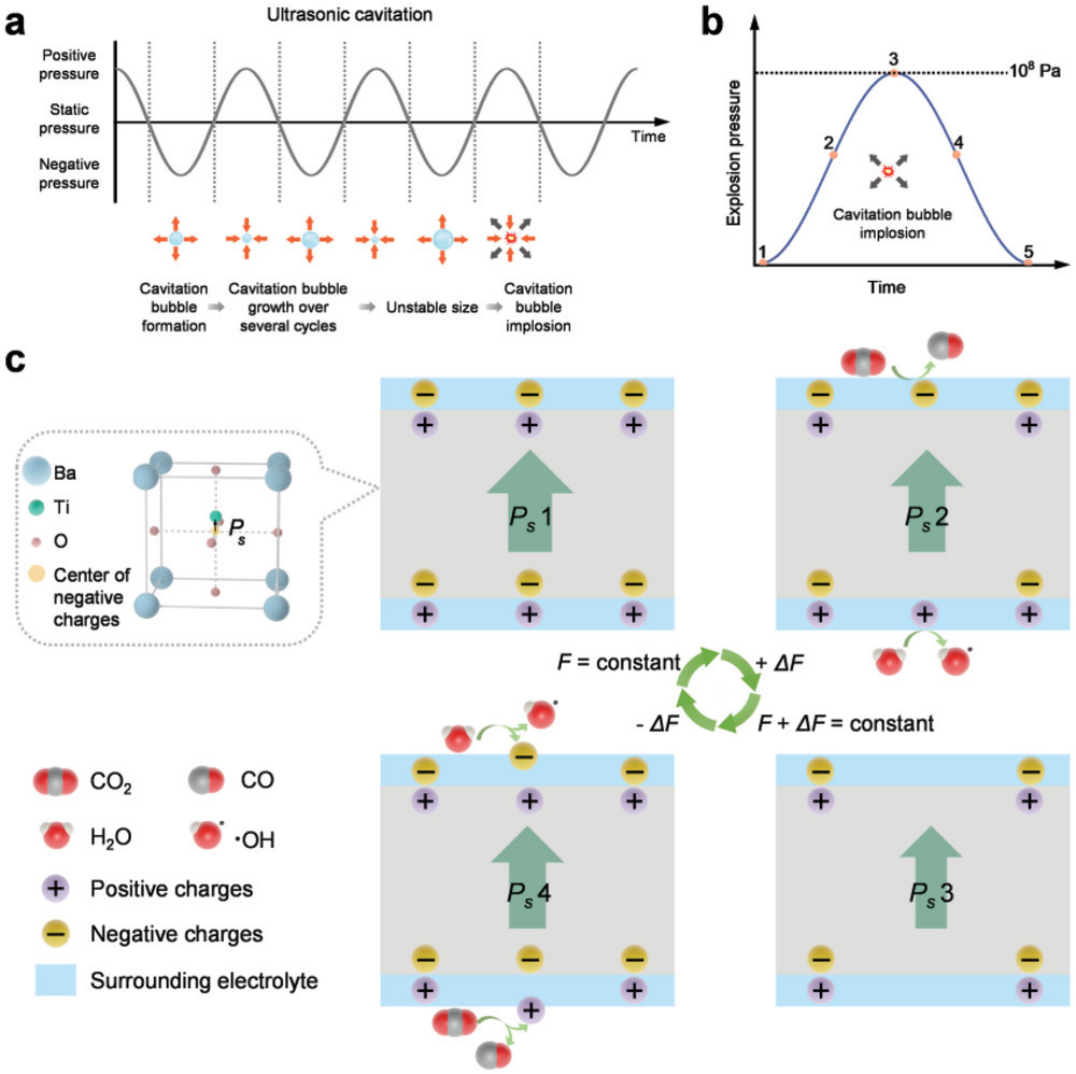

Figure 3. Piezo-electrocatalytic CO_2 reduction reaction process. (**a**) Formation of the driving stress originating from ultrasonic cavitation used in piezo-electrocatalysis. (**b**) Cavitation bubble implosion. (**c**) Mechanism of PECRR using $BaTiO_3$. (Reprinted with permission from Ref. [47]. Copyright 2022, Wiley-VCH).

3. Intrinsic Superiorities of MOFs Applied in Piezocatalysis

Compared with inorganic and polymeric piezoelectric counterparts, the core unique merit of MOFs lies in artificially tunable crystallographic inversion symmetry, which enables continuous regulation of spontaneous dipole intensity and strain-triggered surface shielding charge density. This chapter divides MOFs advantages into two interconnected categories: intrinsic piezo-ferroelectric lattice properties directly controlled by symmetry breaking, and auxiliary catalytic structural features optimizing solid–liquid mass transfer kinetics. Both sets of merits synergistically enhance overall piezocatalytic performance. Table 1 summarizes the intrinsic superiorities of MOFs materials for piezocatalysis from two dimensions, namely intrinsic piezoelectric tunability and auxiliary catalytic structural merits, covering thermal-response properties, aqueous chemical stability and versatile synthetic feasibility for device construction.

Table 1. Summary of intrinsic superiorities of MOFs materials for piezocatalytic applications.

Superiority Category	Specific Feature	Physical/Chemical Origin	Contribution to Piezocatalysis
Intrinsic piezoelectric tunability	Negative linear compressibility (NLC) effect	Counter-intuitive wine-rack-type topological behavior: hydrostatic compression triggers expansion along one crystallographic axis while total unit-cell volume decreases	Amplifies lattice deformation magnitude under mechanical excitation, thus enhancing intrinsic piezoelectric polarization output for piezocatalysis
Intrinsic piezoelectric tunability	Flexible organic linker torsion	Reversible torsion, bending and swing of organic ligands under cyclic stress	Adds extra local dipole oscillation and contributes to displacement-current generation
Intrinsic piezoelectric tunability	Controllable lattice defect polarization	Missing linkers and coordinatively unsaturated metal sites break local centro-symmetry	Nucleates localized polarization domains and strengthens space-charge screening effects
Intrinsic piezoelectric tunability	Tunable Curie temperature and broad thermal operation window	Tunable d-π orbital hybridization strength between metal centers and organic linkers, combined with intrinsic framework thermal stability	Sustains spontaneous lattice dipoles under fluctuating working temperatures and adapts to biomedical and industrial thermal-fluctuating operating scenarios
Auxiliary catalytic structural merits	Excellent acid–base chemical durability	High-valent-metal carboxylate/low-valent-metal azolate coordination bonds	Resists lattice collapse in acidic, neutral, and alkaline aqueous piezocatalytic environments and improves long-term cyclic stability
Auxiliary catalytic structural merits	Ultrahigh specific surface area and porosity	Periodic porous framework constructed from metal nodes and organic linkers	Exposes abundant surface active sites and accelerates interfacial mass transport and substrate adsorption
Auxiliary catalytic structural merits	Abundant and tailorable active sites	Dual active sites from both metal-node centers and functionalized organic linkers	Precisely adjusts adsorption free energy of reaction intermediates and optimizes catalytic reaction pathways
Auxiliary catalytic structural merits	Band structure engineering feasibility	Reticular chemistry enables modular tuning of ligand and metal-node electronic states	Matches redox potentials of diverse reactions
Auxiliary catalytic structural merits	Mild and diversified synthetic routes for device integration	Versatile solvothermal/microwave/room-temperature synthesis under ambient-pressure low-temperature conditions	Facile fabrication of powders, single crystals and self-standing films and lower technical barrier toward device assembly

3.1. Intrinsic Piezo-Ferroelectric Properties Enabled by Symmetry Engineering

3.1.1. Piezoelectric Descriptors: Definitions, Units, and Comparability

Piezoelectric coefficients are core physical parameters for evaluating piezoresponse, yet different descriptors represent distinct physical quantities and cannot be directly interchanged. Careful consideration of measurement principles is required for cross-literature comparison.

The direct and converse piezoelectric coefficients (d_{33}), with units of pm V^{-1} or pC N^{-1} (numerically equivalent), describe the charge generated per unit applied mechanical force under the direct piezoelectric effect, or the strain induced per unit applied electric field under the converse piezoelectric effect along the polar axis. The voltage coefficient (g_{33}) is defined as $g_{33} = d_{33}/\varepsilon_0\varepsilon_r$, with the unit of V m N^{-1}. It quantifies the electric field produced under applied mechanical stress, and its value is inversely correlated with the dielectric permittivity of the material. A high g_{33} value does not guarantee strong charge generation capacity, as it may originate from a low dielectric constant even with a moderate d_{33}.

Macroscopic measurement approaches such as the Berlincourt method and resonance spectroscopy can obtain intrinsic piezoelectric coefficients of bulk materials. In contrast, piezoresponse force microscopy (PFM) provides an effective tip-calibrated piezoresponse signal denoted as d_{33}. This effective value is affected by multiple experimental factors, including contact stiffness, tip radius, driving frequency and contact resonance conditions. Thus, PFM-derived d_{33}^* is suitable only for relative comparison within a single study, and direct comparison across different instruments or literature reports is not reliable.

Remanent polarization P_r, extracted from ferroelectric P–E hysteresis loops, characterizes the residual polarization state of ferroelectric domains after removing the external electric field. It reflects ferroelectric switching behavior rather than being an intrinsic piezoelectric coefficient.

Piezopotentials acquired from KPFM characterization or COMSOL simulation are strongly dependent on sample geometry, boundary conditions, and the local electrostatic screening environment. These values represent simulated or measured local electrostatic potentials instead of intrinsic material constants.

Given the above differences, quantitative cross-study comparison in this review is restricted to catalytic reaction rates measured under clearly defined mechanical excitation conditions. For piezoelectric descriptors, comparisons are only performed among results obtained using identical measurement techniques.

3.1.2. Controllable Piezoelectric and Ferroelectric Responses

Crystallographically, there exists a strict hierarchical relationship among the 32 crystallographic point groups. The 11 centrosymmetric point groups contain an inversion center and are neither piezoelectric nor pyroelectric nor ferroelectric. Among the remaining 21 non-centrosymmetric point groups, 20 exhibit piezoelectric character (point group 432 is the sole exception where symmetry elements cancel piezoelectric responses). It should be emphasized that non-centrosymmetry is a necessary yet insufficient condition for spontaneous macroscopic polarization. Only 10 out of these 21 non-centrosymmetric point groups are polar point groups, which host a unique polar axis and give rise to pyroelectricity (temperature-dependent spontaneous polarization). Ferroelectrics represent an even narrower subclass within polar crystals: ferroelectric materials must possess switchable spontaneous polarization that can be re-oriented between symmetry-equivalent states by an external applied electric field. Accordingly, non-centrosymmetric MOFs structures may exhibit purely piezoelectric characteristics without possessing pyroelectric or ferroelectric properties [49–52]. All ferroelectric materials intrinsically integrate piezoelectric, pyroelectric, and second-harmonic generation (SHG) effects, and numerous MOFs systems have been verified to exhibit polar and ferroelectric-related switching behaviors. It is worth emphasizing that porous, ionic, and defect-rich MOFs commonly contain mobile ions and space-charge regions, which can produce extrinsic electrostatic signals that mimic electromechanical responses. For this reason, qualitative PFM amplitude butterfly loops, phase hysteresis, and P–E loop features alone cannot serve as definitive evidence for intrinsic ferroelectric or piezoelectric behavior. Reliable identification of intrinsic polar switching requires multi-faceted validation, including frequency-dependent PFM measurements, DC-poling-induced phase reversal, off-field retention tests, leakage-current correction for electrical characterization, and complementary crystallographic and SHG verification [38]. A wealth of MOFs systems has been validated to deliver ferroelectric or piezoelectric activity [53–56].

Sun's group first offered experimental confirmation of ferroelectric signatures within UiO-66 nanocrystals [38]. Combined experimental characterizations and theoretical simulations revealed that structurally modulated UiO-66 variants yield distinguishable piezoresponse (PR) hysteresis curves via piezoresponse force microscopy (PFM). Moreover, UiO-66(Hf) nanocrystals display far more prominent piezoelectric switching performance relative to their Zr-based UiO-66 analogs. Back in 2017, Sun and coworkers further probed the piezoelectric traits of NUS-6 nanocrystals by utilizing dual AC resonance tracking piezoresponse force microscopy coupled with piezoresponse force spectroscopy (DART-PFM) [57]. Figure 4 presents DART-PFM images (1 μm × 1 μm) of NUS-6(Hf) (Figure 4a–d) and NUS-6(Zr) (Figure 4e–h). Figures 4a and 4e show AFM topographic images that record the surface morphology of NUS-6(Hf) and NUS-6(Zr), respectively. The corresponding PFM amplitude

maps (Figure 4b,f) reflect the magnitude of local electromechanical signals. larger values of d_{zz} = 2.0–3.5 pm V^{-1} were determined for NUS-6-(Hf) nanocrystals, which were much larger than those of NUS-6-(Zr) (1.5–2.5 pm V^{-1}) (Figure 4c,g). Three-dimensional reconstructed amplitude plots (Figure 4d,h) further intuitively reveal the PFM amplitude image overlaid on the topographic image for both NUS-6-(Hf) and NUS-6-(Zr) nanocrystals, respectively. Such PFM characterizations demonstrate heterogeneous electromechanical signals on the sample surface, where amplitude indicates locally switchable polar domains. It should be emphasized that these signals represent effective tip-calibrated piezoresponse, which may be interfered with by mobile ions and space-charge effects inherent to porous MOFs. Therefore, these PFM mappings provide qualitative evidence of local polar behavior rather than definitive proof of intrinsic ferroelectricity. In 2020, Roy and co-workers reported a three-dimensional MOF constructed from cadmium metal nodes and isoniazid (INH) organic linkers, with the chemical composition denoted as CdI_2-INH=CMe_2 [58]. This material achieves a piezoelectric charge coefficient of ~143 pC N^{-1}, which is around 4.5 times greater than that of commercial piezoelectric polyvinylidene difluoride (PVDF) thin films. In 2025, Sankalpa N. Panda obtained the metal–organic framework $Cu_4I_4(Pip)_2$ via room-temperature crystallization, where Cu_4I_4 cubane-type SBUs are cross-linked by piperazine linkers [59]. This MOF adopts the non-centrosymmetric space group P6222. Using switching-spectroscopy piezoresponse force microscopy (SS-PFM) and PFM for crystal imaging, they investigated its strong piezoelectricity and measured a d_{33}^* of ~52.33 pm V^{-1}, revealing its potential for mechanical-energy harvesting. Yang et al. reported that negative linear compressibility (NLC) boosts the dynamic piezoelectric response of Ni(PyC)$_2$·DMF (IISERP-MOF2; PyC = 4-pyridinecarboxylate, DMF = N,N-dimethylformamide). The NLC along the crystallographic b-axis induces substantial strain along the c-axis, yielding a piezoelectric coefficient g_{33} of 859.4 × 10^{-3} V m N^{-1}, which is 75.6-fold higher than $BaTiO_3$ and 2.8-fold higher than poly(vinylidene fluoride) (PVDF) [52]. Importantly, this mechanism was further validated in two additional MOFs and one NLC-active molecular framework. Devices fabricated from MOF/polymer composites delivered outstanding performance in energy harvesting and underwater ultrasonic sensing, reaching 1.4 times and 2.4 times the efficiency of $PbZr_xTi_{1-x}O_3$ and PVDF-based counterparts, respectively. This paradigm demonstrates that large piezoelectric effects can be realized in diverse non-centrosymmetric NLC crystals.

3.1.3. Tunable Curie Temperature and Broad Thermal Operation Window

Curie temperature (T_C) is defined as the critical temperature threshold at which materials lose intrinsic spontaneous polarization dipoles and surface-bound charges, representing a universal bottleneck restricting the practical application of conventional ferroelectric inorganic materials. Statistical analysis of global ferroelectric databases reveals that over 95% of reported ferroelectrics possess T_C values below room temperature, and merely 26 candidates exhibit T_C exceeding 127 °C, severely limiting their stable catalytic performance in temperature-fluctuating industrial and environmental scenarios [60]. Benefiting from their tunable coordination structures, the Curie temperature of MOFs can be artificially elevated by strengthening d−π orbital hybridization between metal centers and organic linkers, enabling stable retention of spontaneous dipoles and surface-bound charges over a wide temperature range [61]. Typical Cr-based coordination frameworks well illustrate this regulation mechanism: the pristine Cr(pyz) MOF delivers a low T_C of 71 °C, while rational linker modification strengthens metal-ligand hybridization, raising the T_C of Cr(diphos)$_2$ to 239 °C and Cr(diarse)$_2$ to 164 °C. In addition, MOFs exhibit excellent thermal decomposition stability under inert atmospheres, with MIL-53 maintaining intact lattice structures above 500 °C, UiO-66 stable up to 500 °C, and MIL-100 decomposing at approximately 270 °C [62–64]. Although the absolute thermal decomposition temperature of MOFs is

lower than that of high-melting-point perovskite oxides, most piezocatalytic reactions proceed in aqueous media near ambient temperature. For genuinely ferroelectric MOF piezocatalysts, the Curie temperature, rather than the decomposition temperature, is the relevant thermal figure of merit because it marks the loss of the switchable spontaneous polarization that sustains the piezopotential. For non-ferroelectric piezoelectric MOFs, which constitute the majority of the systems compiled in this review, T_C is not defined and must not be used as an evaluation index; their practical temperature window is instead limited by aqueous chemical stability, temperature-induced structural phase transitions, guest-molecule escape, mechanical fatigue under cyclic strain, and framework decomposition. Under the fluctuating-temperature conditions of wastewater remediation and industrial vibration catalysis, the practical evaluation of these MOFs should therefore rely on the above structural and chemical stability constraints rather than on the Curie temperature.

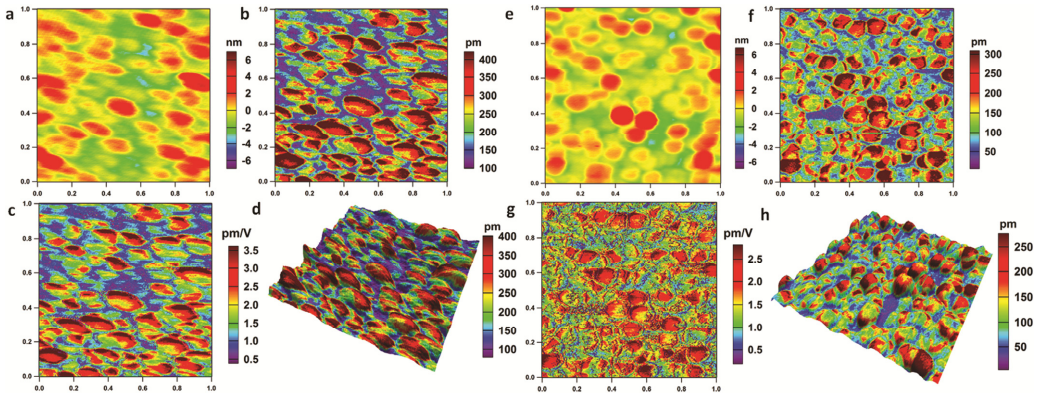

Figure 4. DART-PFM images (1 μm × 1 μm) of NUS-6-(Hf) (**a**–**d**) and NUS-6-(Zr) (**e**–**h**) nanocrystals: (**a**,**e**) topography; (**b**,**f**) amplitude; (**c**,**g**) d_{zz}; and (**d**,**h**) 3D image of amplitude overlaid on topography image. (Reprinted with permission from Ref. [57]. Copyright 2017, Royal Society of Chemistry.

3.2. Auxiliary Catalytic Structural Superiorities Optimizing Mass Transfer & Interfacial Reaction

The structural advantages elaborated in this subsection cannot directly regulate lattice spontaneous dipoles or piezopotential magnitude, but they effectively optimize the solid–liquid reaction microenvironment and accelerate interfacial catalytic kinetics after strain-induced polarization and band bending formation, offering excellent chemical durability, high-efficiency pore mass transfer performance, and facile synthetic compatibility.

3.2.1. Outstanding Acid–Base Chemical Durability in Complex Aqueous Media

Long-term cyclic piezocatalytic pollutant degradation and energy conversion reactions are generally implemented in acidic, neutral, or alkaline aqueous environments, making chemical structural stability a fundamental prerequisite for recyclable catalytic operation. The pH tolerance of MOFs is precisely determined by their coordination bonding modes: high-valent metal-carboxylate coordination bonds endow frameworks with prominent acid resistance, while low-valent metal-azolate coordination systems deliver excellent alkali stability. Classic MOF systems fully validate this unique property. ZIF-8, constructed by Zn-imidazolate bonds, retains complete crystallinity after long-term boiling treatment in an 8 M strong alkaline solution [65]. Similarly, Zr-carboxylate-based UiO-66 maintains intact lattice integrity across an ultra-wide pH range of 1–14 [66]. Such exceptional universal pH stability fundamentally addresses the irreversible lattice collapse issue of conventional inorganic oxide piezocatalysts during long-cycle aqueous catalysis, greatly extending the service life of MOF piezocatalysts in complex practical water systems, including river water, industrial wastewater, and seawater. This robust chemical durability also supports the application of MOFs in harsh acidic CO_2 aqueous reduction systems for clean energy conversion.

3.2.2. Ultrahigh Porosity and Large Specific Surface Area to Multiply Active Interfaces

Traditional inorganic piezoelectric materials suffer from dense stacking structures and limited specific surface areas, which severely restrict their catalytic performance. The insufficient surface area leads to scarce pollutant adsorption sites and limited charge accumulation space, fundamentally hindering piezocatalytic reaction kinetics. In sharp contrast, reticular self-assembly endows MOFs with permanent interconnected pore channels and ultra-large specific surface areas. This unique structural advantage lays a solid foundation for high-efficiency pollutant mineralization and clean energy conversion applications. Yang and co-workers described a new class of high-efficiency piezoelectric composites based on a PVDF matrix, in which $Co_3[Co(CN)_6]_2$ MOF was introduced as the functional filler [67]. Benefiting from its ultra-large specific surface area and intrinsic open-pore nanostructure, $Co_3[Co(CN)_6]_2$ is capable of triggering pronounced interfacial coupling inside the PVDF host, giving rise to improved piezoelectric outputs. Furthermore, redox-active metallic centers within the MOF facilitate electron migration channels, which may further intensify interfacial interactions and contribute to superior piezoelectric amplification. The composite reaches its optimum piezoresponse at a filler content of 0.6 wt% $Co_3[Co(CN)_6]_2$, yielding d_{33} = 37 pC N^{-1} and d_{31} = 33 pC N^{-1}, values nearly twice as large as those of bare PVDF.

3.2.3. Mild, Diversified Synthetic Routes Convenient for Device Integration

Conventional inorganic piezoelectric ceramics require high-temperature calcination above 1000 °C, accompanied by high energy consumption and cumbersome preparation procedures, which greatly limit their scalable fabrication and device integration. In comparison, MOFs piezocatalysts can be synthesized via diverse mild strategies, including solvothermal reaction, microwave irradiation, room-temperature co-precipitation, and sonochemical synthesis under low-temperature and atmospheric-pressure conditions [68–70]. Benefiting from the wide availability of commercial organic linkers and common inorganic metal salts, MOFs synthesis features low raw material cost and simple operation. More importantly, one-pot synthetic routes enable the direct preparation of MOFs powders, bulk single crystals, and self-supporting flexible films without secondary high-temperature post-treatment. Such mild and versatile synthetic technologies significantly lower the industrial scaling and device integration threshold of MOFs piezocatalysts compared with traditional piezoelectric ceramics. Nevertheless, the high cost of chiral or fluorinated functional ligands and the reliance on toxic high-boiling solvents still hinder the large-scale green manufacturing of high-performance MOFs piezocatalysts.

3.2.4. Easily Tailored Molecular Structures

Experimental investigations have verified that functional-group grafting represents a facile and feasible strategy for tailoring MOF architectures while retaining their outstanding thermal and chemical stabilities [71,72]. Owing to their exceptionally tunable molecular frameworks, these MOF materials hold great promise for boosting piezocatalytic reaction efficiency and broadening their application scope under harsh operational conditions. Accordingly, unraveling the inherent structure-property correlation is indispensable for advancing the catalytic performance of MOF-based piezocatalysts. Rationally targeted design further enables the precise implantation of desired active sites into MOF lattices at the atomic scale.

To ameliorate piezoelectric features, a set of M-doped Co-gallate compounds (M = Mg, Mn, Ni) has been successfully fabricated. Recorded electrical hysteresis loops disclose divergent piezoelectric responses, confirming substantially upgraded performance relative to pristine Co-gallate [73]. Mg-doped Co-gallate delivers a two-fold enhancement in remanent polarization, whereas Mn-doped and Ni-doped counterparts attain six-fold and four-fold increments, respectively. Such elevated piezoelectric behaviors stem from enhanced global

structural polarity triggered by framework distortion upon hetero-metal incorporation. Likewise, Zr^{4+} cations were introduced into parent MOF-802(Hf) to manipulate its local structure and further upgrade its piezoelectric functionalities, yielding the Zr-modified MOF-802(Hf) series [74]. The Zr-doped product exhibits well-defined P-E hysteresis loops, solid evidence for its piezoelectric nature, with markedly superior performance compared with unmodified MOF-802(Hf). At a Zr^{4+} doping level of 5%, the remanent polarization reaches 0.511 $\mu C\ cm^{-2}$, unambiguously demonstrating robust piezoelectric activity. This value surpasses that of the undoped parent material and is competitive against several well-established perovskite-type piezoelectrics.

From the above perspective, the high structural tailorability of MOFs confers great merits for the exploration, analysis, and iterative optimization of piezocatalytic catalysts. Moreover, the structural flexibility intrinsic to MOF systems permits diversified material construction through fine-tuning of building-block components, which in turn modulates their collective contributions toward piezocatalytic processes.

4. Multi-Level Symmetry Hierarchy Modulation Strategies of MOFs for Enhanced Piezocatalytic Activity

Combining the intrinsic piezo-tunability and auxiliary structural merits of MOFs outlined in Section 3, this chapter discusses multiple modification routes that can give rise to symmetry-associated piezocatalytic effects. It establishes a logically progressive three-tier symmetry-engineering hierarchy ranging from intrinsic atomic-lattice modification and metal-mediated dipole amplification to heterogeneous-interface synergistic construction. It should be emphasized that these approaches do not uniformly alter bulk crystallographic inversion symmetry. Before detailing individual strategies, four physically distinct classes of symmetry-related modification must be distinguished, as they act on different structural levels and do not imply one another. Critically, piezocatalytic performance gains reported in the literature may originate either from these symmetry-altering effects or from simultaneously altered confounding variables, including surface area, pore geometry, defect density, adsorption affinity, electrical conductivity, band-edge position, and particle morphology. Disentangling symmetry contributions from these co-varying material properties requires well-matched centrosymmetric reference samples and multi-condition excitation experiments.

(i) Bulk crystallographic symmetry breaking: a change in the crystal space group itself (e.g., conversion of a centrosymmetric parent into a non-centrosymmetric or polar space group), which alters symmetry-allowed property frameworks across the entire crystal lattice.
(ii) Local coordination/defect symmetry breaking: symmetry lowering confined to secondary building units, linkers, or defect sites (polar ligand grafting, lattice vacancies, post-synthetic metal coordination), while the average space group of the parent lattice remains unchanged.
(iii) Surface or interfacial inversion asymmetry: inversion-asymmetric conditions emerging at heterojunctions. Built-in electric fields and polarization discontinuities are interfacial properties, whereas the bulk MOF component may still retain its original inversion center.
(iv) Morphological/strain anisotropy: facet exposure, rod-versus-flake topology, or porosity gradients that redistribute strain and bound-charge distribution, without necessarily modifying the bulk crystal space group.

Each modulation route below first elaborates on its corresponding symmetry-modulation category and working mechanism, followed by supporting experimental cases.

Table 2 summarizes the classification, structural features, representative MOF examples, and corresponding references for the aforementioned multi-level symmetry modulation strategies, offering a quick-reference overview before detailed case discussions.

4.1. Atomic-Scale Intrinsic Lattice Symmetry Engineering

General symmetry-breaking principle: Modify single-metal coordination skeletons via linkers, metal nodes, or vacancies to produce local lattice asymmetry without introducing foreign heterogeneous phases. Three orthogonal sub-strategies are classified.

4.1.1. Polar Functional Ligand Grafting

Polar ligand grafting exclusively refers to covalent modification of organic linker backbones by incorporating polar substituent groups (–NH_2, adenine moieties, –NO_2, fluorinated groups) to break local crystallographic centrosymmetry and generate intrinsic strain-responsive dipoles. This route focuses purely on chemical functionalization of organic ligands, excluding metal node replacement and morphological tuning.

Zhu and co-workers prepared NH_2-MIL-101(Fe) via a hydrothermal route. Combined piezoelectric force microscopy (PFM) and electrochemical analyses demonstrated that amino (-NH_2) moieties promoted the electron-transfer kinetics of MIL-101(Fe), which contributed to the ameliorated piezocatalytic performance [75]. Ding et al. prepared metal–organic frameworks UiO-66 and UiO-66-NH_2, and systematically characterized their piezoelectric behaviors via PFM. Upon mechanical agitation, the strongly polarized UiO-66 and UiO-66-NH_2 function as electron donors to reduce aryl diazonium salts and yield aryl radical intermediates. Among the examined substrates, UiO-66-NH_2, with superior piezoelectric performance, afforded higher reaction efficiency relative to unmodified UiO-66 [76]. To further amplify lattice asymmetry, adenine with multi-amino coordination sites was co-introduced as a modified linker to fabricate AD-U Zr-MOF [77]. PFM piezoresponse hysteresis curves directly verified the drastically elevated surface piezopotential of AD-U compared with unmodified UiO-66. The multi-amino polar linker shortened RhB and diclofenac removal to merely 60 min, achieving elimination efficiencies of 93% and 98%, respectively. Nitro-substituted ligand derivatization represents another classic polar grafting strategy for Fe-based frameworks. Ding's group synthesized NO_2-MIL-101(Fe) using –NO_2 functionalized benzene dicarboxylate linkers [78]. Well-defined butterfly-shaped piezoresponse amplitude hysteresis loops are acquired for BDC-MOF and NO_2-BDC-MOF, with the nitrated-ligand sample exhibiting larger amplitude. Fluorinated ligand grafting further expands the library of polar linker modifications. Zhao's team utilized tetrafluoroterephthalate as a fluorinated polar linker to construct UiO-66-F_4, where F substituents break lattice symmetry and enhance framework flexibility [79]. Figure 5 illustrates the piezocatalytic hydrogen evolution performance and mechanism of fluorine-modified UiO-66 MOF. Figure 5a presents the cyclic piezocatalytic H_2 production curves of pristine UiO-66 and UiO-66-F_4 under ultrasonic vibration. Bare UiO-66 exhibits negligible hydrogen generation, while UiO-66-F_4 delivers a stable and much higher H_2 yield over three consecutive cycles, demonstrating that fluorine substitution greatly enhances the piezocatalytic activity. Figure 5b schematically depicts the piezocatalytic hydrogen evolution process of UiO-66-F_4: ultrasonic vibration induces piezoelectric polarization within the framework, which drives water reduction to produce H_2. Figure 5c shows the calculated reaction energy profiles for H_2 evolution. The energy barrier for H* intermediate formation on UiO-66-F_4 is much lower than that of pristine UiO-66, confirming that fluorine modification optimizes the HER thermodynamics. Figure 5d displays the crystal structure of UiO-66-F_4, in which fluorine atoms are introduced onto the organic linkers to break the centrosymmetry of the parent UiO-66 framework. Notably, the enhanced piezoresponse and piezocatalytic activity originate from symmetry breaking after fluorine functionalization. The UiO-66-F_4 developed by Zhao's group also achieves ~95% RhB degradation over a 3 h reaction period [80].

Table 2. Quantitative comparison of multi-level symmetry hierarchy modulation strategies.

Symmetry Hierarchy Modulation Strategies	Structural Modification	MOFs Piezocatalyst Example	Reaction	Experimental Conditions	Mechanical Stress Source	Catalytic Performance	Reference
Polar Functional Ligand Grafting	–NH_2 functional linker	NH_2-MIL-101(Fe)	Degradation	Catalyst dosage = 0.2 g L^{-1}, CIP initial concentration = 5 mg L^{-1}	Ultrasonic Transducer (100 W, 100 kHz)	87.4% in 60 min	[75]
Polar Functional Ligand Grafting	–NH_2 functional linker	UiO-66-NH_2	Organic synthesis	Aryldiazonium tetrafluoroborate dosage = 0.30 mmol, bis(pinacolato)diborane dosage = 0.30 mmol, UiO-66-NH_2 catalyst dosage = 120 mg, DMF dosage = 0.23 or 0.27 μL/mg, milling jar volume = 5.0 mL	Ball Milling (Retsch MM 400, 30 Hz)	78% in 1 h	[76]
Polar Functional Ligand Grafting	Adenine co-linker	AD-U	Degradation	20 mg catalyst dispersed into the DCF or RhB solution (10 mL L^{-1}, 60 mL)	Stirring	RhB and DCF 93% and 98% in 60 min	[77]
Polar Functional Ligand Grafting	–NO_2 substituted linker	NO_2-MIL-101(Fe)	Degradation	50 mg of catalyst in 100 mL of TC aqueous solution (20 mg/L)	100 kHz, 70 W	95% in 30 min	[78]
Polar Functional Ligand Grafting	Tetrafluorinated linker	UiO-66-F_4	H_2 production	20 mg catalyst dispersed in 15 mL Na_2SO_3 (1 mol L^{-1}) and 85 mL water	40 kHz, 110 W	178.5 μmol/g in 5 h	[79]
Polar Functional Ligand Grafting	Tetrafluorinated linker	UiO-66-F_4	Degradation	20 mg of catalyst in 100 mL of RhB aqueous solution (10 mg/L)	40 kHz, 110 W	85% in 3 h	[80]
Isostructural Metal Node Tuning	Zr/Hf substitution	UiO-66-NH_2(Zr), UiO-66-NH_2(Hf)	H_2 production	10 mg of catalyst, 30 mL of CH_3CN, 200 μL of deionized water, 600 μL of TEA, Pt is 1 wt% of the catalyst	200 W, 53 kHz, 300 W Xe lamp with a UV cut-off filter (>380 nm)	0.74 mmol g^{-1} h^{-1}, 1.61 mmol g^{-1} h^{-1}	[40]
Isostructural Metal Node Tuning	Zr/Hf/Ce screening	X-UiO-66 (X = Zr, Hf, Ce)	H_2O_2 production	50 mg catalyst dispersed in 50 mL of pure water with ethanol (10 vol%)	180 W, 40 kHz + 900 rpm stirring	0.83 mmol g^{-1} h^{-1}, 0.54 mmol g^{-1} h^{-1} 0.13 mmol g^{-1} h^{-1}	[81]
Isostructural Metal Node Tuning	Fe, Cr	MIL-101(Cr), MIL-101(Fe)	H_2O_2 production	2 mg catalyst dispersed in 10 mL of pure water with ethanol (10 vol%)	100 W, 40 kHz	2.76 mmol g^{-1} h^{-1}, 1.31 mmol g^{-1} h^{-1}	[82]
Morphology regulation	Rod vs. flake topology	FCAU-17, CAU-17	Degradation	100 mg of catalyst dispersed in 5 mg L^{-1} of 100 mL RhB solution	300 W, 40 kHz	78.6%,90.1% in 80 min	[83]
Lattice Vacancy Construction	Missing-linker defects	Vacancy-rich UiO-66	H_2 production	50 mg catalyst dispersed in 4 mL MeOH (1 mol L^{-1}) and 16 mL water, $AgNO_3$ is the co-catalyst	240 W, 40 kHz	39.6 μmol/g/h	[84]
Metal-Mediated Lattice Dipole Amplification	Gradient Zr–Hf doping	UiO-66-NH_2(Zr–Hf)	Degradation	50 mg of catalyst in 50 mL of RhB aqueous solution (40 mg/L)	180 W, 40 kHz, 400 W metal halide lamp	96.78% in 30 min	[85]
Metal-Mediated Lattice Dipole Amplification	Hf_xZr_{6-x} solid clusters	UiO-66(Hf_xZr_{6-x})	H_2O_2 production	20 mg catalyst dispersed in 100 mL water	320 W, 40 kHz	4.8 mmol g^{-1} h^{-1}	[86]
Metal-Mediated Lattice Dipole Amplification	Post-Synthetic Transition Metal Coordination Grafting	Cu-NH_2-MIL-125	H_2 production	10 mg of catalyst, 10 mL of CH_3CN, 180 μL of deionized water, 10 mL of TEA, Pt is 1 wt% of the catalyst	300 W, 50 kHz, 300 W Xe lamp with a UV cut-off filter (>380 nm)	2.88 mmol g^{-1} h^{-1}	[87]

Table 2. *Cont.*

Symmetry Hierarchy Modulation Strategies	Structural Modification	MOFs Piezocatalyst Example	Reaction	Experimental Conditions	Mechanical Stress Source	Catalytic Performance	Reference
Metal-Mediated Lattice Dipole Amplification	Post-Synthetic Transition Metal Coordination Grafting	Cu-UiO-66-NH_2	H_2 production	20 mg of catalyst, 10 mL of CH_3OH, 90 mL of deionized water	300 W, 45 kHz,	1.38 mmol g^{-1} h^{-1}	[88]
Metal-Mediated Lattice Dipole Amplification	Post-Synthetic Transition Metal Coordination Grafting	Ni-UiO-66-NH_2	H_2 production	2 mg of catalyst, 1 mL of CH_3OH, 9 mL of deionized water	300 W, 40 kHz,	17.61 mmol g^{-1} h^{-1}	[89]
Metal-Mediated Lattice Dipole Amplification	Post-Synthetic Transition Metal Coordination Grafting	Cu-UiO-66-NH_2	Methanol production	20 mg of catalyst, 10 mL of water, 10 vol% CH_4 in N_2 and O_2 (100 mL·min^{-1})	360 W, 40 kHz,	0.175 mmol g^{-1} h^{-1}	[90]
Heterostructure Construction	Binary MOF-Inorganic Semiconductor Hybrids	Fe-BTC/$BiFeO_3$ and Cu-BTC/$BiFeO_3$	Degradation	20 mg of catalyst dispersed in 5 mg L^{-1} of 80 mL NFX solution	20 W, 20 kHz	49.7%,60.2% in 60 min	[91]
Heterostructure Construction	Binary MOF-Inorganic Semiconductor Hybrids	BiOCl/UiO-66	H_2 production	50 mg of catalyst, 2 mL of CH_3OH, 18 mL of deionized water	120 W, 40 kHz	0.65 mmol g^{-1} h^{-1}	[92]
Heterostructure Construction	Binary MOF-Inorganic Semiconductor Hybrids	Bi_2O_2Se@Bi-MOF	H_2O_2 production	10 mg of catalyst, 5 mL of EtOH, 45 mL of deionized water	100 W, 53 kHz	1965.9 μmol g^{-1} h^{-1}	[93]
Heterostructure Construction	Binary MOF-Inorganic Semiconductor Hybrids	Zr-MOF/carbon nitride	H_2O_2 production	2 mg of catalyst, 20 mL of deionized water	300 W, 40 kHz	4.76 mmol g^{-1} h^{-1}	[94]
Heterostructure Construction	Core–shell inorganic@MOF	MOF@SnSe	Benzyl alcohol oxidation	25 mg of catalyst, 3 mg of 4-aminobenzenyl alcohol, 10 mL of deionized water	90 W, 45 kHz	604.3 μmol g^{-1} h^{-1}	[95]
Heterostructure Construction	Core–shell organic@MOF	VBiTO-10@NU-66	HCHO oxidation	75 mg of catalyst, 5 mL of simulated gas	480 W, 45 kHz	95.1% in 3 h	[96]
Heterostructure Construction	Core–shell organic@MOF	DABT@UiO	Degradation	10 mg of catalyst dispersed in 10 mg L^{-1} of 10 mL ENR solution	Air pressure (0.2 MPa)	90.0% in 150 s	[97]
Heterostructure Construction	Ternary multi-phase heterostructure	ZnO/CuO@UiO-66-NH_2	Degradation	50 mg of catalyst dispersed in 10 mg L^{-1} of 50 mL RhB solution	mechanic agitation	99.7% in 30 min	[98]
Heterostructure Construction	Polymer-MOF monolithic heterodevices	PVA-PPy-gelatin-UiO-66-F_4	Degradation	small piece of the PPGUM-HG3 dispersed in 10 mg L^{-1} of MB solution	vortex-induced mechanical stress	96% in 60 min	[99]
Heterostructure Construction	Polymer-MOF monolithic heterodevices	PDA@UiO-66-NH_2(Hf)/PVDF	Degradation	3 × 3 cm^2 of catalyst dispersed in 10 mg L^{-1} of 30 mL RhB solution	150 W, 40 kHz	97.9% in 40 min	[100]
Heterostructure Construction	Polymer-MOF monolithic heterodevices	BWO@CAU-17/PVDF	Degradation	5 cm of catalyst dispersed in 5 mg L^{-1} of 50 mL RhB solution	80 W, 40 kHz	90.3% in 80 min	[101]

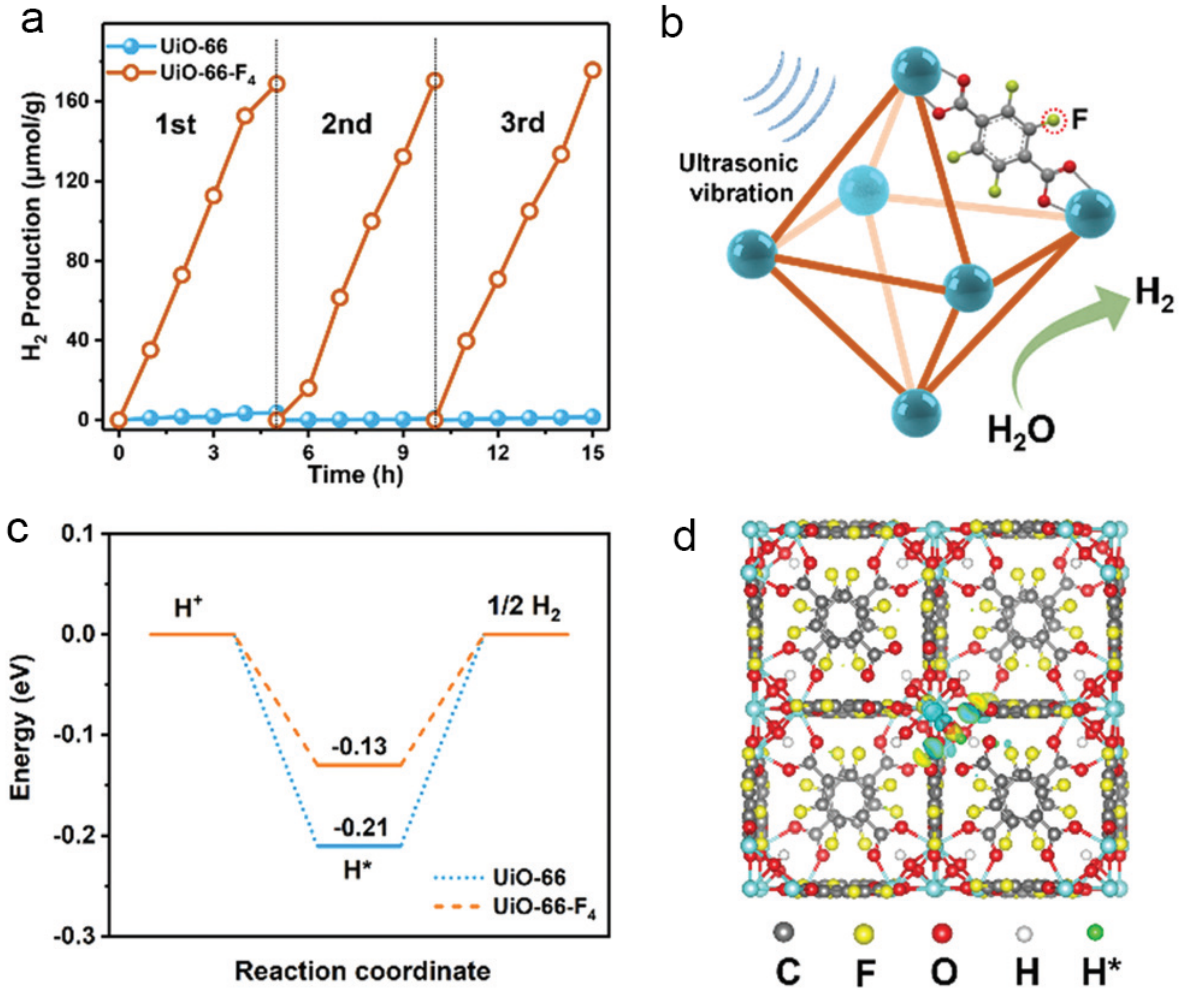

Figure 5. (**a**) Three cycles of time-dependent H_2 evolution curves over UiO-66 and UiO-66-F_4 under ultrasonic vibration. (**b**) Schematic illustration of the mechanism of piezocatalytic H_2 production from water over the UiO-66-F_4 via harvesting vibration energy. (**c**) Gibbs free energy (ΔGH*) diagram for hydrogen adsorption on UiO-66 and UiO-66-F_4. (**d**) Most stable atomic configurations of hydrogen adsorption on UiO-66-F_4 (Reprinted with permission from Ref. [79]. Copyright 2022, Royal Society of Chemistry).

Comparative analysis of the above five polar-ligand systems permits the symmetry contribution to be discriminated from confounding variables. All five cases retain the topology and metal nodes of their parent frameworks, so differences in surface area, pore geometry, and particle morphology are secondary; the dominant variables are the number and electronic nature of the polar substituents. Electron-donating groups (-NH_2, adenine) simultaneously raise the linker HOMO level and introduce permanent local dipoles: NH_2-MIL-101(Fe) and AD-U both exhibit PFM-verified increases in piezopotential, and AD-U, which carries multiple amino coordination sites, delivers the strongest polarization and the fastest pollutant removal, indicating that dipole density rather than ligand polarity per se controls the response. The electron-withdrawing -NO_2 group lowers linker electron density yet still enlarges the piezoresponse amplitude, demonstrating that substituent-induced local symmetry breaking is the common physical origin, while band-edge shifts and adsorption changes are strategy-specific parallel consequences. Fluorination instead acts mainly through framework softening (enhanced linker torsion and negative-linear-compressibility character); i.e., it improves strain-transfer efficiency rather than the static dipole moment. Two caveats qualify these conclusions. First, none of these studies rigorously decouples symmetry breaking from the defect density concurrently introduced during grafting, so a fraction of the activity gain may be defect-mediated rather than purely symmetry-derived.

Second, all performance tests were conducted under strong ultrasonic protocols, so the reported improvements describe activity under intense excitation, and their persistence under low-grade vibration remains unverified. Excitation-resolved comparisons with defect-matched, centrosymmetric controls are therefore a prerequisite for establishing genuine symmetry-activity design rules.

4.1.2. Metal Node Substitution and Dimensional Morphology Regulation

Distinct from ligand grafting, this subcategory modulates lattice polarization via two orthogonal approaches: isostructural replacement of metal SBUs within identical linker backbones, and dimensional morphology engineering of single-metal frameworks. Both strategies retain unchanged organic linkers and thus cannot be classified as ligand modification routes.

Isostructural Metal Node Tuning

Under fixed polar ligand environments, substitution of metal cluster centers adjusts metal–ligand orbital hybridization strength to amplify overall lattice polarity. In 2021, Zhang et al. compared the piezo-photocatalytic performance of isostructural UiO-66-NH_2(Zr) and UiO-66-NH_2(Hf) with identical amino linkers [40]. As illustrated in Figure 6a, the schematic compares the photo-piezocatalytic behavior of Zr-based and Hf-based UiO-66-NH_2 under combined ultrasonic and light excitation. Replacing Zr with Hf in the metal node brings an obvious improvement in catalytic activity. Under coupled light–ultrasound excitation, the Hf-node analog delivered 2.2-fold higher hydrogen evolution activity, while the two materials exhibited nearly identical pure photocatalytic performance without vibration, confirming that Hf–linker orbital coupling strengthens strain-induced polarization. Yuan et al. systematically screened X-UiO-66 (X = Zr, Hf, Ce) with consistent terephthalate backbones, identifying Hf-UiO-66 with a piezoelectric coefficient of 1.1 nm V^{-1} and a piezocatalytic H_2O_2 production rate of 827.6 μmol g^{-1} h^{-1} [81]. Figure 6b presents the structural diagram of the Hf-containing secondary building unit, showing the coordination environment of Zr/Hf/Ce centers linked by organic ligands. Mechanistic analysis revealed that Hf node substitution optimizes two-electron oxygen reduction kinetics via intensified lattice polarization.

Further comparative analysis of isostructural defective MIL-101(Cr) and MIL-101(Fe) verified that Cr metal centers possess stronger electron-donating capacity and piezoelectric ability to amplify piezocatalytic H_2O_2 yield [82]. PFM phase-voltage and displacement-voltage hysteresis curves are displayed for MIL-101(Fe) in Figure 6c and for MIL-101(Cr) in Figure 6d. A larger maximum piezoelectric displacement of 20.1 nm is observed for MIL-101(Cr), whereas MIL-101(Fe) delivers a displacement value of 17.2 nm, which demonstrates that metal-center substitution can directly alter the piezoelectric response amplitude. To interpret such metal-dependent behavior, Figure 6e summarizes the underlying electronic mechanism originating from different metal-site electronegativity. Fe sites possess stronger electronegativity and tend to act as electron acceptors with relatively stable electronic states. By contrast, Cr sites exhibit weaker electronegativity and serve as electron donors with more active electronic configurations. Under ultrasonic stimulation, strain-induced charge carriers participate in successive oxygen reduction pathways. With ethanol as the sacrificial reagent, defective MIL-101(Cr) reaches a production rate of 2.76 mmol g^{-1} h^{-1}, which is 2.11 times higher than its Fe analog.

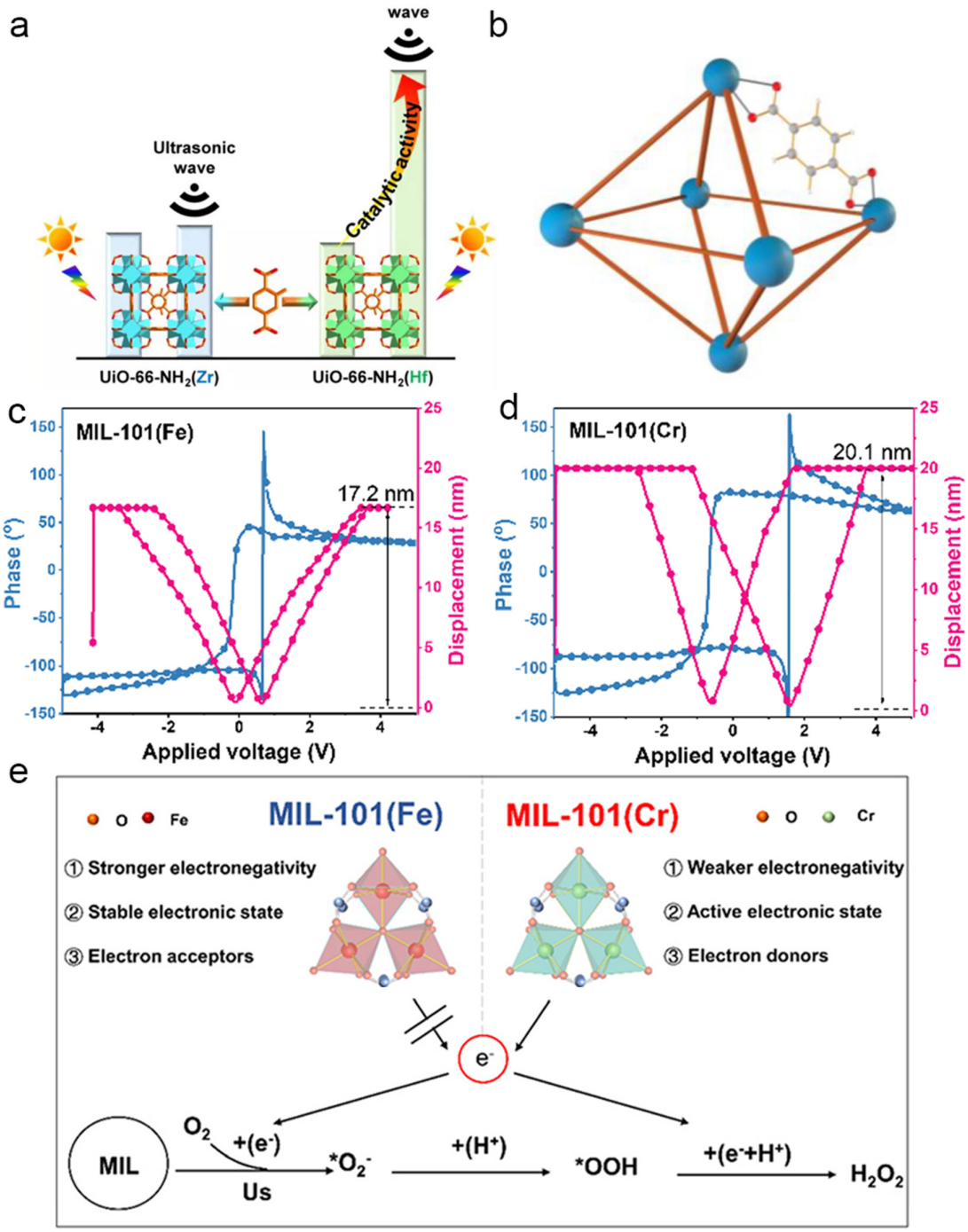

Figure 6. (**a**) Piezocatalytic activity comparison between UiO-66-NH_2(Zr) and UiO-66-NH_2(Hf) (Reprinted with permission from Ref. [40]. Copyright 2021, Wiley-VCH GmbH); (**b**) Atomic cluster structure of Hf/Zr SBU (Reprinted with permission from Ref. [81]. Copyright 2025, Wiley-VCH GmbH); (**c**,**d**) PFM phase-displacement hysteresis loops of MIL-101(Fe) and MIL-101(Cr); (**e**) Electronic structure difference between Fe-based and Cr-based MIL frameworks and the corresponding piezocatalytic H_2O_2 generation pathways (Reprinted with permission from Ref. [82]. Copyright 2023, Royal Society of Chemistry).

Comparative analysis of these isostructural metal node substitution systems helps to disentangle symmetry polarization contributions from confounding material variables. Even with unchanged organic linkers and framework topology, metal node replacement can subtly modify defect population, d-π orbital hybridization, band edge positions, and textural properties, including pore volume, which co-determine final piezocatalytic output.

Across the tested UiO-66 and MIL-101 families, Hf- and Cr-based analogs deliver stronger piezoresponse relative to Zr- and Fe-isotypes, which is partially ascribed to intensified metal-ligand orbital coupling that amplifies local lattice polarity. Nevertheless, it remains difficult to fully isolate polarization effects from concurrent band structure modulation without isostructural reference samples with precisely matched defect density and specific surface area. Most reported comparisons rely on ultrasonic high-power excitation; whether the observed metal-node-dependent piezoresponse persists under low-grade ambient vibration still requires further verification. Matching property isostructural controls combined with multi-regime mechanical excitation are necessary to establish definitive structure-activity rules for metal node tuning strategies.

Dimensional and Topological Morphology Engineering

Morphology regulation manipulates strain, deformability, and exposed asymmetric crystal facets without altering ligand or metal node composition. Bi-based monometallic MOFs further exhibit morphology-dependent piezoresponse. Rod-shaped CAU-17 and flaky FCAU-17 can be fabricated from identical trimesic acid linkers and $Bi(NO_3)_3$ precursors by adopting distinct crystallization protocols [83]. Rod-shaped CAU-17 exposes abundant asymmetric crystal planes and delivers ~90% RhB degradation within 80 min, with band alignment perfectly matched for $\bullet O_2^-$ and •OH radical generation.

For morphology-modulated MOF piezocatalysts, morphological anisotropy redistributes local strain and exposes asymmetric crystal facets without altering intrinsic crystal space group symmetry. It is important to distinguish strain redistribution-derived piezocatalytic improvements from parallel changes in specific surface area, facet-dependent reactant adsorption, and carrier transport behavior. The rod-shaped CAU-17 exhibits superior performance compared with its flaky counterpart, yet the relative contributions from strain anisotropy versus enlarged active interfacial area have not been quantitatively separated in original work. At present, morphology-related piezocatalysis studies rarely report surface area-normalized kinetic rates. To validate that performance gains originate from strain redistribution rather than simply higher accessible surface sites, future experiments should adopt surface area-normalized activity metrics alongside centrosymmetric morphological reference samples under identical mechanical excitation.

4.1.3. Controllable Lattice Vacancy Construction

Precise introduction of lattice vacancies, which include missing organic linkers and coordinatively unsaturated metal sites, erases the native centrosymmetry of stoichiometric monometallic MOFs lattices and nucleates localized polarization domains. Defect engineering creates intrinsic lattice asymmetry independent of ligand functionalization or metal substitution. Yu et al. successfully regulated the piezoelectric response of UiO-66-NH_2 (Hf, Zr) through simple acetic acid (AA) modification and observed that the piezoelectric response showed an upward trend with the increase in AA dosage (Figure 7a). During the synthesis, single carboxylate groups were introduced into the missing-linker defects, which significantly changed the structure of MOFs. The introduction of modifiers broke the original high symmetry of MOFs, thereby improving their piezoelectric performance. This work opens up a new avenue for regulating the piezoelectric response of existing MOFs through structural modulation for further study of piezoelectric MOFs [102]. Wang and colleagues adopted defect-controlled UiO-66 as a canonical model to quantify vacancy-mediated piezoelectric enhancement [84] (Figure 7b–d). PFM characterizations revealed a 6.25-fold elevation in piezoelectric coefficient for vacancy-rich UiO-66 relative to defect-free crystals. Molecular dynamics simulations attributed this amplification to flexoelectric polarization emerging near vacant lattice sites. Integrated piezocatalytic hydrogen evolution tests,

electrochemistry, and DFT calculations collectively elucidated a synergistic mechanism: vacancies facilitate rapid charge separation, accelerate carrier mobility, and lower hydrogen adsorption energy barriers. Under identical ultrasonic conditions, defective UiO-66 delivers nearly twice the hydrogen production rate of intact UiO-66.

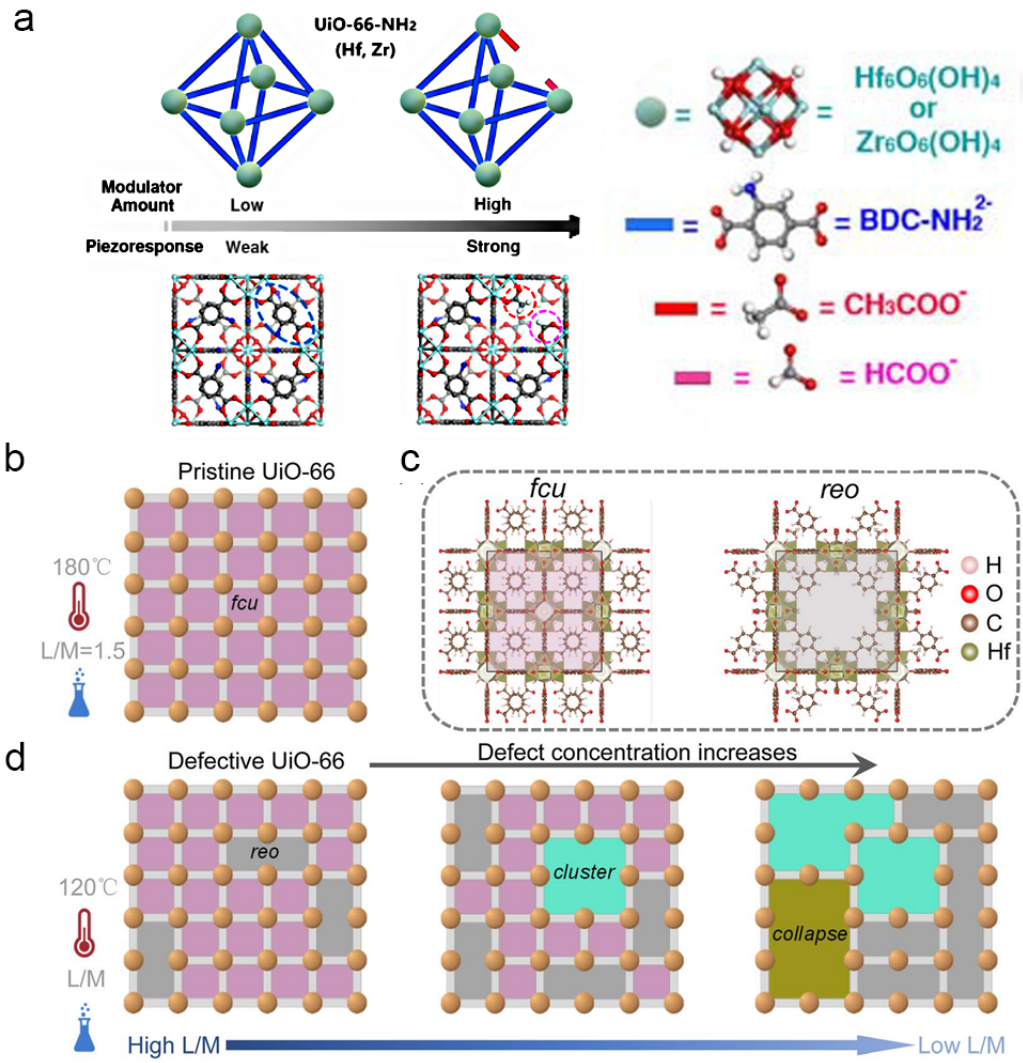

Figure 7. (**a**) Effect of modulator dosage on defect generation and piezoresponse of UiO-66-NH_2 (Hf, Zr) (Reprinted with permission from Ref. [102]. Copyright 2025, Royal Society of Chemistry). (**b**) The synthetic conditions employed to synthesize pristine UiO-66 crystals with a defect-free fcu topology. (**c**) Atomic models of 12-connected fcu topology and 8-connected reo topology of UiO-66. (**d**) Evolution of reo domains in synthesized crystals induced by changes in superlattice diffraction and cluster connectivity with varying L/M ratios (Reprinted with permission from Ref. [84]. Copyright 2026, Royal Society of Chemistry).

Vacancy-introducing defect engineering generates local symmetry-breaking flexoelectric polarization inside MOFs lattices; however, vacancy formation simultaneously alters multiple confounding material properties. Missing-linker defects produce coordinatively unsaturated metal sites, increase electrical conductivity, modify pore geometry, and change mass-transfer kinetics. In vacancy-rich UiO-66, the observed enhancement in piezoelectric coefficient and hydrogen-evolution rate represents a combined consequence of local symmetry lowering, improved carrier mobility, and additional exposed active sites. Current literature seldom decouples these intertwined effects: most studies lack well-defined, defect-free centrosymmetric reference samples with matched surface area for direct comparison. Moreover, defect concentration is difficult to precisely quantify and reproduce

across different synthetic batches. To quantify the true fraction of performance originating from symmetry-induced flexoelectric polarization, researchers require quantitative defect characterization paired with defect-matched centrosymmetric controls and multi-condition mechanical excitation tests.

4.2. Metal-Mediated Lattice Dipole Amplification

General symmetry-breaking principle: Introduce heterogeneous metal coordination environments inside or outside MOF lattices to create large-scale charge imbalances and further amplify overall lattice dipoles, divided into in situ bimetallic SBU alloying and post-synthetic metal coordination grafting.

4.2.1. In Situ Bimetallic Secondary Building Unit

Although atomic-scale symmetry modulation of single-metal MOF skeletons can substantially boost piezocatalytic activity, the adjustable range of intrinsic lattice polarity is inherently constrained by fixed monometallic coordination environments. To address this limitation, the bimetallic node alloying strategy introduces heterogeneous metal coordination sites into isostructural MOFs backbones, breaking the uniform intralattice charge equilibrium of single-metal frameworks and generating asymmetric internal charge redistribution. Such heterogeneous lattice polarization drastically amplifies the overall framework dipole magnitude and elevates the density of strain-triggered surface-bound charges. By precisely tuning the molar stoichiometry of dual-metal secondary building units (SBUs), synchronous optimization of pore geometric parameters, semiconductor band alignment, and piezoelectric coefficient can be realized simultaneously, striking a balanced trade-off between lattice polarization strength and interfacial carrier separation. At present, only a limited library of single-metal MOFs has been exploited for piezocatalysis, and their overall catalytic performance remains insufficient for practical deployment, driving research efforts to incorporate multi-metal sites to elevate catalytic efficiency and diversify available piezocatalytic platforms. A series of quantitative experimental investigations have fully validated the unique advantages of bimetallic node modulation, and two representative isostructural Zr/Hf bimetallic UiO systems deliver distinct mechanistic insights into cluster symmetry breaking [85]. Prior compositional studies centered on amino-functionalized bimetallic UiO-66-NH_2(Zr–Hf) frameworks with gradient Hf doping ratios. Textural characterizations further revealed that specific surface area, pore volume, and average pore diameter exhibit a monotonic declining trend with increasing Hf ion doping content. The UN(0.75 Zr) sample possessed the maximum pore volume and average pore size, which facilitates sufficient substrate adsorption and interfacial mass transport. These observations unambiguously demonstrate that metal stoichiometry exerts equally critical impacts on piezocatalytic performance as metal identity, and rational compositional tuning is indispensable to maximize catalytic throughput.

Consistent with this compositional dependence, prior comparative analysis confirmed that Hf^{4+} nodes give rise to intensified metal–ligand orbital hybridization and aggravated lattice distortion relative to Zr^{4+} [40]. Complementing pollutant degradation-oriented Zr/Hf amino-MOFs, Wang and co-workers establishes a generalized cluster-symmetry-breaking strategy to endow intrinsically centrosymmetric UiO-66 with prominent piezocatalytic activity for green H_2O_2 synthesis [86]. Bimetallic metal-cluster substitution serves as an effective strategy to break the intrinsic centrosymmetry of UiO-66 and induce local polarization. As presented in Figure 8a, isomorphous substitution of partial Zr^{4+} by Hf^{4+} within the metal cluster disrupts the highly symmetric monometallic framework and generates asymmetric bimetallic UiO-66 with missing-cluster features. Figure 8b compares the local configuration of symmetric Zr-only clusters and asymmetric Hf-Zr mixed clusters.

The introduction of Hf sites creates separated positive and negative charge centers and produces an intrinsic local polarization vector within the secondary building unit. The theoretical charge-distribution maps for a series of Hf-Zr heterometallic clusters are displayed in Figure 8c. Corresponding quantitative charge-difference statistics in Figure 8d demonstrate that the Hf_1Zr_5 cluster yields the maximum net charge difference (Δ_{Charge} = 0.037 e), implying the strongest local polarization among these heterometallic combinations. Beyond hetero-metal doping, linker-missing defects can also bring about local charge separation. Figure 8e illustrates that missing-linker defects generate positive charge centers at metal clusters and negative centers at defect sites along the [100] crystallographic direction, which gives rise to additional built-in polarization. DFT calculated charge values for perfect UiO-66 and defective bimetallic UiO-66 are summarized in Figure 8f. The formation of defect-induced negative centers further redistributes surface charge and reinforces the internal polarization field of the bimetallic framework, which is favorable for enhancing piezocatalytic charge-separation efficiency.

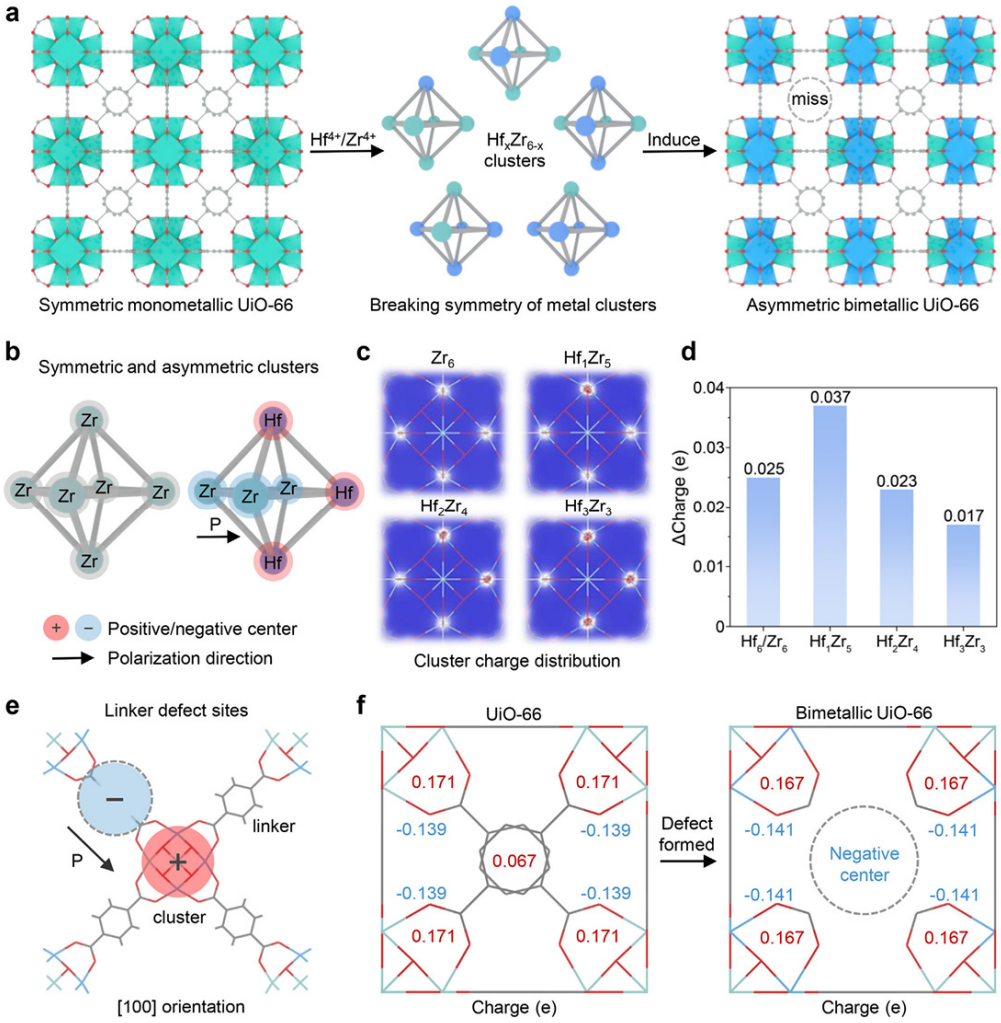

Figure 8. Design and theoretical prediction of symmetry breaking of UiO-66. (**a**) Schematic diagram of symmetry breaking engineering in bimetallic UiO-66 for enhancing piezoelectric polarization. (**b**) Mechanism of polarization induced by charge asymmetry in metal clusters. (**c**,**d**) Charge distribution along [100] orientation of Zr_6, Hf_1Zr_5, Hf_2Zr_4, and Hf_3Zr_3 clusters, and the corresponding charge difference. (**e**) Mechanism of polarization caused by linker defects in bimetallic UiO-66(Hf_3Zr_3) crystal structure. (**f**) Charge distribution and negative center formation at linker defect sites in UiO-66(Hf_3Zr_3) (Reprinted with permission from Ref. [86]. Copyright 2026, Wiley-VCH GmbH).

Bimetallic SBU alloying disrupts the uniform charge equilibrium of monometallic SBUs, creating local asymmetric charge distributions and amplifying lattice dipoles. The introduction of chemically dissimilar metal centers into secondary building units disturbs the homogeneous electrostatic environment of monometallic frameworks. Heterometallic atomic sites with varying electronegativities induce offset charge-accumulation and charge-depletion regions within clusters, which gives rise to intrinsic local dipoles under external mechanical strain and strengthens strain-responsive polarization. However, variations in metal stoichiometry also modify pore parameters, surface area, defect density, and band alignment as confounding variables. These intertwined structural and electronic alterations frequently co-occur with the local symmetry breaking originating from bimetallic mixing. Consequently, it remains challenging to attribute observed piezocatalytic enhancements solely to dipole amplification induced by heterometallic SBU construction. Without well-matched monometallic reference samples possessing comparable pore structures, defect concentrations, and band positions, it is difficult to quantitatively decouple the contribution of lattice dipole enhancement from other concurrent material variations. Most existing experimental investigations tune metal molar ratios without strictly controlling these interfering factors, which may lead to ambiguous interpretations of the structure-activity relationships for bimetallic MOFs piezocatalysts.

4.2.2. Post-Synthetic Transition Metal Coordination Grafting

Although ligand functionalization and intrinsic vacancy engineering can effectively break centrosymmetric lattices and boost the piezoresponse of single-metal MOFs, such strategies are limited to modulating the polarity of pristine coordination skeletons without introducing independent extrinsic polarization centers. Post-synthetic metal coordination modification emerges as a universal, mild structural tuning strategy: exogenous transition metal ions (Cu, Ni, Co) are anchored onto amino nitrogen, lattice defect sites, or open metal sites of pre-synthesized polar MOFs via metal–N/O coordination bonds. This strategy retains the original topology of parent MOFs, permanent pore channels, and inherent piezoelectric lattices, while constructing heterogeneous interfacial electrostatic domains through mismatched orbital energy levels between the host framework and grafted metal species. Upon mechanical vibration, synergistic coupling between intrinsic lattice polarization and coordination-induced interfacial built-in electric fields drastically elevates the density of uncompensated surface-bound charges, accelerates electron–hole dissociation, and suppresses rapid carrier recombination. Meanwhile, coordinated metal sites serve as multi-functional redox-active centers, synchronously optimizing the thermodynamics of target catalytic reactions, including methane partial oxidation and piezocatalytic water splitting. A series of systematic experimental, PFM spectroscopic, and theoretical computational studies have verified the universal efficacy of metal coordination tuning for amplifying framework intrinsic dipoles, covering Ti-, Zr/Hf-based amino-functionalized MOFs platforms with Cu and single-atom Ni coordination modifications.

Hu and coworkers pioneered a dual modulation route integrating amino ligand functionalization and post-synthetic Cu coordination on NH_2-MIL-125 skeletons to synergistically amplify overall lattice polarity, representing the first systematic demonstration of metal coordination tuning for MOFs piezoelectric performance enhancement [87]. PFM quantitative characterization revealed that the piezoelectric coefficient increased sharply from 1.69 pm V^{-1} for pristine MIL-125 to 26.21 pm V^{-1} for Cu-coordinated Cu-NH_2-MIL-125, accompanied by a pronounced elevation of molecular dipole moment from 6.60 D to 25.99 D. The dual modification strategy breaks dual-scale symmetry at both organic linker and metal-coordination interfaces simultaneously. COMSOL electrostatic simulations further validated that Cu–N coordination bonds create localized charge imbalance,

generating extra strain-responsive dipoles and reinforcing charge separation efficiency under mechanical excitation. This dual polarity tuning paradigm establishes a facile blueprint for subsequent transition metal coordination modification of various polar MOF backbones. Building upon Hf-based amino-functionalized UN-66 (UiO-66-NH_2(Hf)) scaffolds, Zhang and co-workers systematically developed a universal transition metal coordination strategy by anchoring Cu, Co, and Ni ions onto exposed –NH_2 sites via transition metal–N coordination bonds to reconstruct lattice dipole distribution [88]. Compared with unmodified UN-66, Cu-coordinated Cu-UN-66 exhibits drastically upgraded piezoelectric properties. Combined piezoresponse characterizations, COMSOL potential simulations, and DFT free-energy calculations confirm that Cu coordination elevates surface piezopotential, accelerates interfacial carrier separation, and optimizes hydrogen adsorption free energy toward thermoneutrality. Benefiting from optimized polarization and catalytic kinetics, Cu-UN-66 delivers an outstanding piezocatalytic hydrogen evolution rate of 1388.88 μmol g^{-1} h^{-1} under 300 W, 45 kHz ultrasonic irradiation, approximately 86.6-fold higher than bare UN-66 (16.03 μmol g^{-1} h^{-1}). Parallel Co-UN-66 and Ni-UN-66 control samples also display significantly improved hydrogen production activity, fully demonstrating the broad universality of transition metal coordination modification for boosting piezocatalytic dipole strength and catalytic throughput.

Beyond conventional ion coordination, atomically dispersed Ni single-atom coordination on UiO-66-NH_2 realizes unprecedented decoupling of piezoelectric polarization and electronic conductivity, resolving the longstanding trade-off dilemma of polar piezocatalysts with low charge transport efficiency. Hao and co-workers demonstrates that asymmetric Ni–N coordination derived from single-atom grafting substantially amplifies lattice asymmetry, lifting the value from 48 pm V^{-1} of pristine UiO-66-NH_2 to 242 pm V^{-1} [89]. Molecular dynamics simulations show that the charge density difference of Ni SAs@UiO-66-NH_2 is in good agreement with static DFT predictions (Figure 9a), which validates that stable pressure-triggered polarization acts as the dominant driving force for piezocatalysis. DFT free-energy computations demonstrate that the preferred hydrogen adsorption sites switch from carbon sites on organic linkers to Ni single-atom centers, delivering an energy barrier of ~0.12 eV under 100 MPa mechanical pressure (Figure 9b). PDOS profiles uncover the electronic structural transformation (Figure 9c,d). This material preserves semiconducting properties when hydrogen is not adsorbed; upon H adsorption, intense H 1s–Ni 3d orbital hybridization initiates a semiconductor-to-metal transition. The full piezocatalytic HER process is illustrated in Figure 9e. Mechanical strain generates polarization to separate charge carriers, and hydrogen adsorption converts the system into a low-resistance metallic phase. The synergy of piezoelectric polarization and adsorption-induced metallization reduces H adsorption–desorption barriers and yields high piezocatalytic HER activity. Benefiting from synergistic polarization enhancement and optimized hydrogen evolution thermodynamics, Ni SAs@UiO-66-NH_2 achieves record piezocatalytic hydrogen yields of 1871 μmol g^{-1} h^{-1} in pure deionized water and 17,613 μmol g^{-1} h^{-1} in methanol-containing sacrificial media, outperforming most reported state-of-the-art MOF piezocatalysts and competing with advanced piezo-photocatalytic benchmark systems. Apart from clean energy water splitting, Cu-coordinated UiO-66-NH_2 (Cu-UiO-66-NH_2) extends metal-coordination-modified piezocatalysts to mild selective methane partial oxidation, integrating piezoelectric strain activation with biomimetic enzymatic catalysis pathways [90]. Under continuous ultrasonic excitation in a flow reactor, Cu-UiO-66-NH_2 delivers a steady methanol production rate of 175.1 μmol g^{-1} h^{-1} with 82% product selectivity, while batch reactor tests afford CO and H_2 yields of 297.4 μmol g^{-1} h^{-1} and 140.6 μmol g^{-1} h^{-1}, respectively. Mechanistic investigations clarify that mechanical vibration drives piezocatalytic H_2O_2 generation, which decomposes into ·OH

radicals to activate inert C–H bonds in dilute methane feedstock (<10%). Cu(II)-OOH intermediates formed at Cu–N coordination sites decompose into selective Cu(II)-O·radical species that facilitate partial oxidation without deep overoxidation into CO_2, offering a unique metal-coordination-tuned piezocatalytic platform for industrial low-concentration methane conversion.

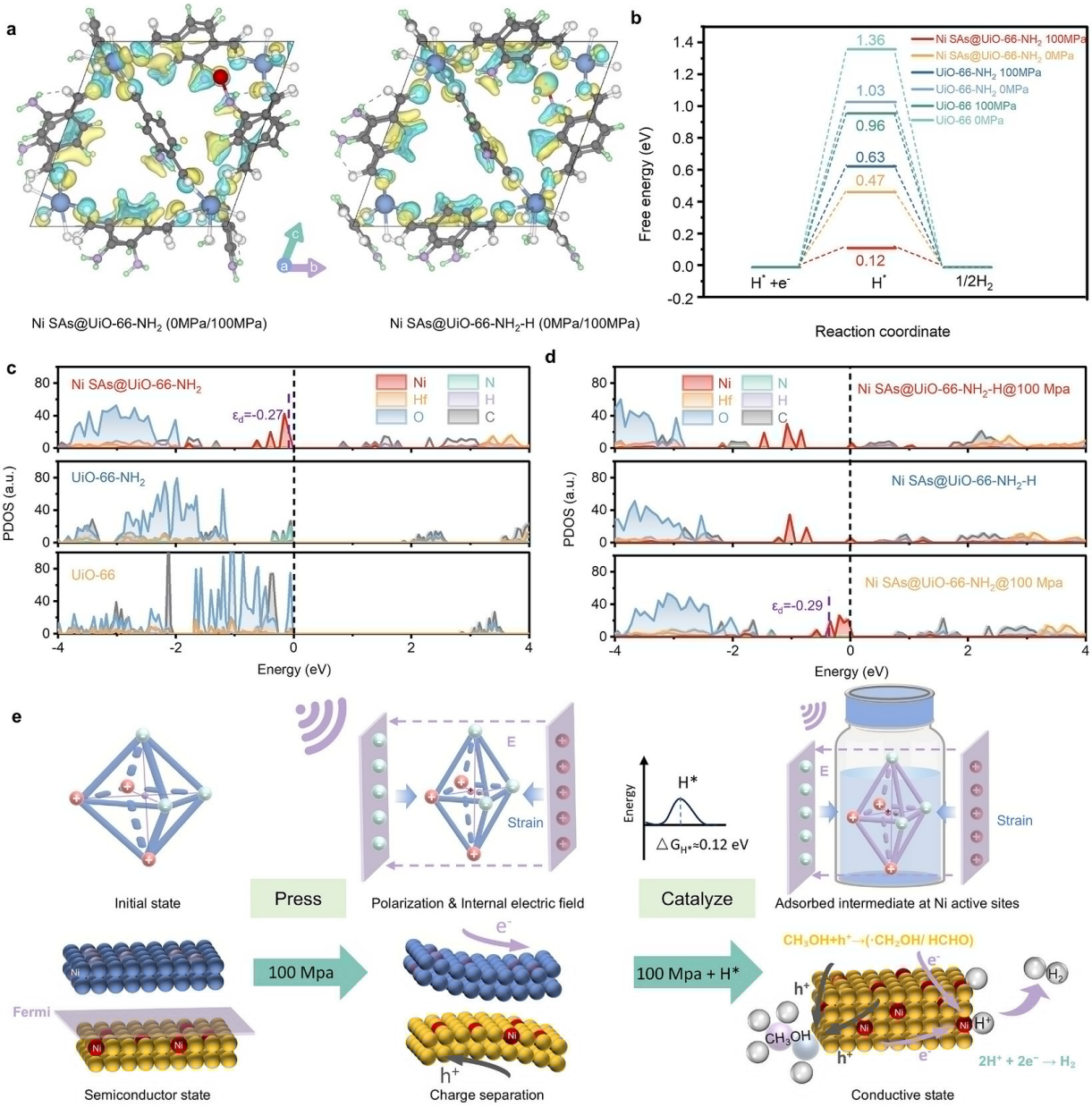

Figure 9. (**a**) Charge density difference maps of Ni SAs@UiO-66-NH_2 and Ni SAs@UiO-66-NH_2–H at 0 MPa and 100 MPa, calculated based on the equilibrium structures obtained from AIMD simulations (yellow and blue regions denote charge accumulation and depletion, respectively); (**b**) Free energy diagrams of different catalysts in the HER process with and without pressure; (**c**) Partial density of states (PDOS) of different systems; (**d**) Partial density of states (PDOS) of Ni SAs@UiO-66-NH_2 under pressure and/or H adsorption (the Fermi level is set to 0 eV); (**e**) The catalytic mechanism of Ni SAs@UiO-66-NH_2 (Reprinted with permission from Ref. [89]. Copyright 2026, Wiley-VCH GmbH).

Collectively, metal coordination modification via post-synthetic transition metal grafting represents a versatile, multi-scenario structural engineering strategy to amplify lattice intrinsic dipoles. By constructing heterogeneous metal–N/O coordination interfaces without destroying parent MOF topology, this approach simultaneously elevates piezoelectric

coefficients, accelerates strain-triggered carrier separation, and tailors redox reaction thermodynamics for diverse applications spanning piezocatalytic hydrogen evolution and selective methane upgrading. Mechanistically, post-synthetic grafting inserts discrete transition metal cations into open nitrogen or oxygen coordination sites, creating localized metal-ligand asymmetric coordination environments that perturb the original centrosymmetric charge distribution. Such heterometallic coordination nodes act as built-in dipole sources under mechanical excitation, intensifying strain-induced polarization and reinforcing the electrochemically active polarization field. Beyond simple dipole amplification, the grafted species concurrently introduce partially occupied d-orbitals that serve as intermediate adsorption sites, thereby modulating the energy landscape of redox reactions and steering reaction selectivity toward specific products such as methane partial oxidation. Experimentally, Cu-ion coordination, single-atom Ni anchoring, and universal Co/Ni metal grafting on amino-functionalized Ti/Zr/Hf MOFs collectively validate the broad adaptability of this symmetry-tuning route, providing rational coordination design guidelines for constructing high-performance, vibration-responsive catalytic materials. Notably, the compatibility of this strategy with diverse metal nodes and linker chemistries implies its applicability beyond the demonstrated families, offering a transferable toolbox for symmetry-oriented MOF engineering.

Nevertheless, several open issues deserve critical attention. First, the precise coordination geometry and oxidation state of grafted metal species are often difficult to characterize unambiguously, and their dynamic stability under continuous mechanical cycling remains insufficiently examined. Second, quantitative disentanglement of dipole amplification from simultaneous changes in surface area, defect population, and band edge positions is rarely achieved, which hinders the establishment of rigorous structure-activity relationships. Third, most evaluations still rely on high-power ultrasonic excitation, whereas performance under low-grade ambient vibration has seldom been verified. Future work should, therefore, combine operando characterization of coordination configuration with isostructural control samples and multi-regime mechanical excitation to consolidate the mechanistic understanding and practical reliability of post-synthetic metal grafting in piezocatalysis.

4.3. Heterostructure Construction

General principle for interface-related symmetry modification: General principles for interfacial asymmetry construction: combine MOFs with other inorganic or organic materials to construct heterogeneous contact interfaces. The resulting interfacial built-in electric field cooperates with the intrinsic symmetry-broken lattice dipoles of MOFs to further separate carriers. Meanwhile, composite interfaces induce new local surface asymmetry in MOFs. Atomic lattice symmetry engineering and post-synthetic metal coordination tuning can effectively boost the intrinsic lattice dipoles of single-component MOFs. Nevertheless, monophasic piezocatalysts inevitably suffer from severe piezo-generated carrier recombination, which fundamentally restricts their overall catalytic kinetics. Heterostructure engineering overcomes this intrinsic limitation by constructing intimate, multi-component contact interfaces. Diverse built-in electric fields emerge at heterogeneous boundaries and synergistically cooperate with strain-induced piezoelectric potentials to accelerate electron-hole separation and suppress charge recombination.

4.3.1. MOFs-Inorganic Semiconductor Hybrids

Binary hybrids combine a single type of MOFs with a separate inorganic piezoelectric/ferroelectric semiconductor, forming simple two-phase heterointerfaces to establish basic charge separation channels without complex multi-component stacking. Taylor Mackenzie Fisher et al. developed two $BiFeO_3$ (BFO)-based binary hybrids integrated with commercial

Fe-BTC and Cu-BTC MOFs, respectively [91]. Electrochemical and optical characterizations confirmed distinct synergistic effects of the two MOF modifiers. Fe-BTC incorporation elevates composite conductivity and light harvesting ability. In contrast, Cu-BTC/BFO achieves 60% NFX degradation under pure piezocatalysis with minimized charge transfer resistance. All electrochemical characterizations verify that MOF modification significantly strengthens interfacial charge transfer and redox capacity compared with bare BFO, providing guidelines for bismuth ferroelectric/MOF advanced oxidation catalysts.

Apart from $BiFeO_3$-based composite systems, BiOCl, another classic bismuth piezoelectric semiconductor, can be coupled with Zr-based UiO-66 to construct efficient binary heterostructures for piezocatalytic hydrogen evolution. Qiu et al. synthesized BiOCl/UiO-66 heterostructures via a facile one-step solvothermal route and systematically assessed their vibration-driven water splitting performance [92]. Under ultrasonic irradiation, the BiOCl/UiO-66 hybrid delivers a prominent hydrogen evolution rate of 650.9 μmol g^{-1} h^{-1}, which far outperforms monocomponent BiOCl (176.5 μmol g^{-1} h^{-1}) and bare UiO-66 (352.6 μmol g^{-1} h^{-1}). The remarkable activity enhancement originates from intimate heterointerface construction: the formed built-in electric field reinforces intrinsic piezoelectric polarization and generates extra exposed active sites, simultaneously facilitating rapid spatial separation of strain-induced charge carriers; furthermore, heterogeneous contact also introduces local interfacial symmetry perturbation at phase boundaries.

Two-dimensional piezoelectric nanosheet-MOF binary heterostructures represent another important subclass for piezocatalytic small-molecule conversion. Xu and co-workers constructed Bi_2O_2Se@Bi-MOF binary hybrids for ultrasonic-driven H_2O_2 synthesis under 53 kHz, 100 W irradiation [93]. The Bi-MOF coating layer simultaneously creates intrinsic interfacial built-in electric fields and enriches surface active sites. Benefiting from the dual synergies of charge separation and surface catalysis, the composite achieves a remarkable H_2O_2 production rate of ~1965.9 μmol g^{-1} h^{-1}, exceeding most reported piezo- and photocatalytic materials.

Beyond bismuth-related piezoelectric systems, carbon nitride can also serve as a piezoelectric substrate to integrate with MOF components. Zhu et al. grafted Zr-MOF onto carbon nitride to construct interfacial electric fields [94]. The piezo-generated internal electric field spatially separates charge carriers. Figure 10a–c present powder XRD patterns, FTIR spectra, and zeta-potential measurements for bare C_3N_4, pristine UiO-66, and the C_3N_4/UiO-66 composite. The XRD results verify the coexistence of characteristic diffraction peaks originating from both components after heterostructure construction (Figure 10a). FTIR spectra confirm the retention of intrinsic functional groups of C_3N_4 and UiO-66 in the composite (Figure 10b). Zeta-potential data reveal opposite surface charges for the two individual materials, which facilitates the formation of intimate interfacial contact (Figure 10c). High-resolution XPS spectra of C 1s, N 1s, and Zr 3d further corroborate the successful fabrication of the C_3N_4/UiO-66 heterostructure and demonstrate interfacial electronic coupling between the two phases (Figure 10d–f). Figure 10 g schematically illustrates the piezocatalytic H_2O_2 production pathway over the C_3N_4/UiO-66 heterojunction. Under ultrasonic agitation, the piezoelectric field generated within the framework couples synergistically with the built-in interfacial electric field, accelerating the spatial separation of charge carriers. The separated holes drive the water oxidation reaction (WOR) to yield H_2O_2, while the electrons participate in the oxygen reduction reaction (ORR) to produce H_2O_2 simultaneously.

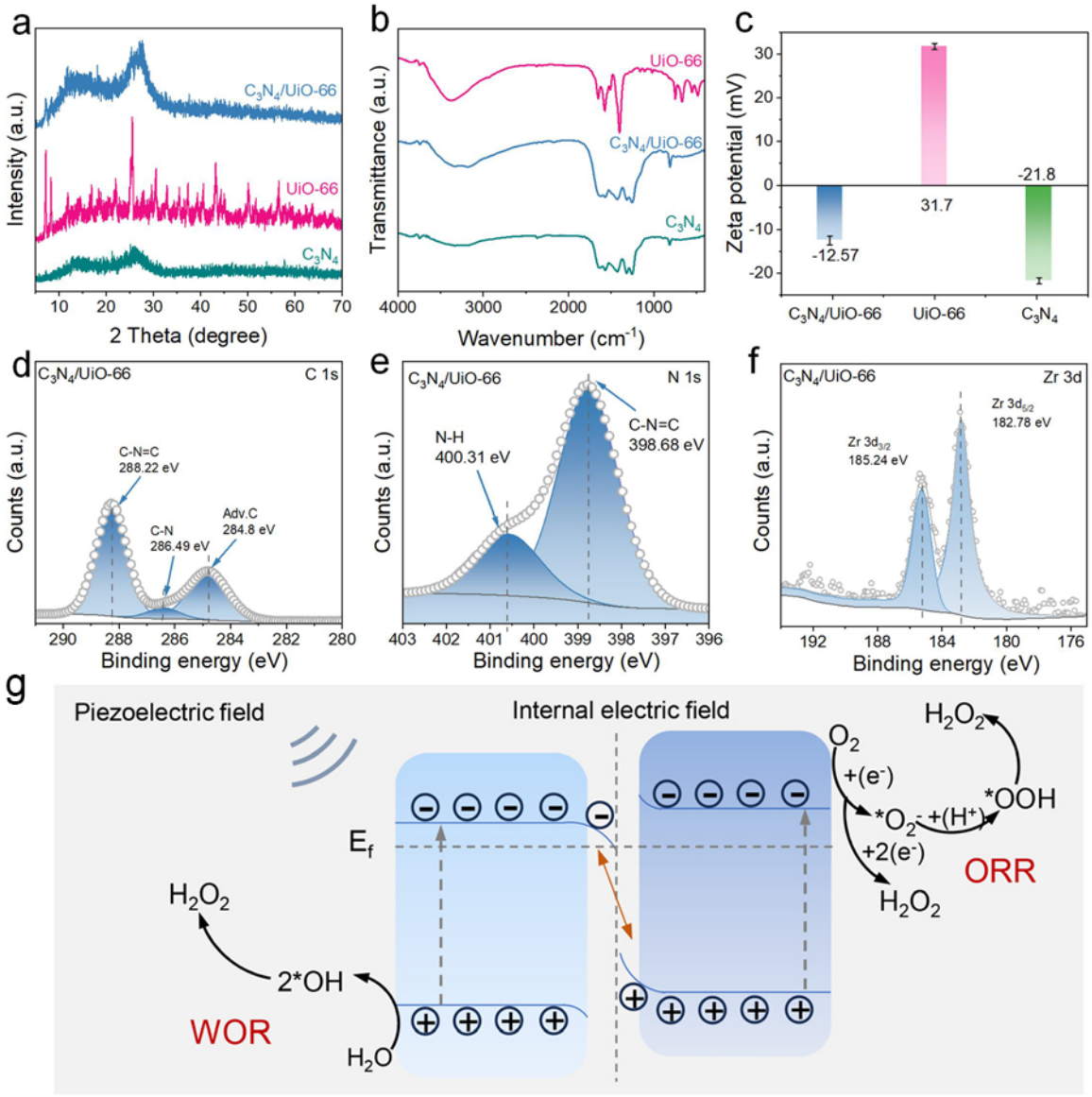

Figure 10. (**a**) XRD patterns, (**b**) FT-IR spectra, and (**c**) zeta potential values of C_3N_4/UiO-66, UiO-66 and C_3N_4. (**d**) C 1s, (**e**) N 1s and (**f**) Zr 3d regions of the XPS spectrum of C_3N_4/UiO-66. (**g**) Proposed reaction mechanism of H_2O_2 production piezocatalyzed by C_3N_4/UiO-66. (Reprinted with permission from Ref. [94]. Copyright 2025, Royal Society of Chemistry).

Liu and co-workers reported amorphous UiO-66-NH_2-coated SnSe 2D nanosheet binary hybrids for selective piezochemical oxidation of organics. Stable interfacial chemical bonds between SnSe and MOF act as high-speed charge transport channels for strain-excited carriers, while the amorphous MOF shell serves as a co-catalyst to lower the formation barrier of ·OH and H_2O_2. Under 90 W, 45 kHz ultrasonication, SnSe/MOF converts benzyl alcohol into benzaldehyde at a rate of 604.3 μmol g^{-1} h^{-1} with 95.3% conversion and >99% selectivity [95]. Vacancy-modified core–shell analogs represented by VBiTO@NU-66 introduce abundant cation vacancies at heterointerfaces to construct fast charge migration pathways [96]. Bi-vacancy-enriched $Bi_4Ti_3O_{12}$ nanosheets coated with UiO-66-NH_2 possess enhanced formaldehyde adsorption via amino groups and amplified lattice polarization from Bi defects. The optimized VBiTO-10@NU-66 achieves 95.1% HCHO oxidation within 3 h. Huang and co-workers pioneered DABT@UiO series organic-inorganic core–shell piezocatalysts [97]. The piezoelectric organic molecule DABT is fully encapsulated within the open pore channels of pristine UiO-66, which inhibits the formation of low-piezoactivity DABT hydrate

in water. Combined with the pollutant enrichment effect of porous MOF and interfacial charge separation of core–shell structures, DABT@UiO-66 degrades 90.0% enrofloxacin within only 150 s with a high rate constant of 0.0172 s^{-1}. By contrast, intermolecular hydrogen bonding between DABT and amino groups in UiO-66-NH_2 causes framework contraction and incomplete DABT encapsulation, leading to deteriorated piezocatalytic performance. This work establishes a tunable strategy by regulating MOF pore openness to fabricate organic piezo-molecule@MOF core–shell catalysts.

Compared with two-component binary hybrid systems, ternary heterojunctions introduce an additional functional component to establish multiple interfacial contacts, which further amplifies built-in electric fields and provides more abundant active sites for piezocatalytic reactions. Guan and co-workers designed a ternary heterojunction structure of ZnO/CuO@UiO-66-NH_2 [98]. A ZnO/CuO heterointerface was constructed on the surface of UiO-66-NH_2 via a hydrothermal method, forming a composite piezoelectric catalytic system with abundant active sites and enhanced built-in electric fields. Under dark conditions, the 30 min degradation rate of RhB by this material reached 99.7%, with a rate constant of 0.09435 min^{-1}, far superior to that of the pure ZnO/CuO system. This work provides new design concepts for the development of efficient and stable heterojunction piezoelectric catalysts and offers potential pathways for the construction of integrated systems for dye wastewater treatment and energy conversion.

4.3.2. Flexible Polymer-MOF Monolithic Devices

Beyond powder-form piezocatalysts, integrating piezoelectric MOFs into polymer matrices to construct flexible monolithic hydrogels and membranes pushes piezocatalysis toward practical device-oriented applications. Richa Kumari and co-workers fabricated flexible PVA-PPy-gelatin-UiO-66(Zr)-F_4 hybrid hydrogels via solvothermal MOF synthesis followed by in situ polymerization and physical crosslinking [99]. PFM characterizations with standard butterfly amplitude loops and 180° phase hysteresis verify intrinsic piezoelectric and converse piezoelectric effects of embedded UiO-66-F_4 crystals. The hydrogel achieves 96% methylene blue degradation (60 min), 92% crystal violet removal (90 min) and 82.5% Cr(VI) reduction (75 min), retaining 87% catalytic efficiency after seven cycles. Radical trapping tests confirm $\cdot O_2^-$ as the dominant reactive species for pollutant mineralization. Yang proposed a polydopamine (PDA) interfacial homogenization strategy to prepare PDA@UiO-66-NH_2(Hf)/PVDF composite piezoelectric membranes [100]. MD simulations reveal strong intermolecular interactions between PDA and PVDF chains that lower the β-phase transition energy barrier. DFT calculations confirm reinforced interfacial bonding between modified MOF and polymer matrix. Introducing PDA@UiO-66-NH_2(Hf) raises polar β-phase PVDF content from 51.0% (pure PVDF) to 66.2%, while simultaneously improving membrane porosity, mechanical strength and hydrophilicity. Mechanical vibration triggers abundant$\cdot O_2^-$ and ·OH generation at heterointerfaces, achieving a stable dye degradation rate constant of 0.107 min^{-1}.

BWO@CAU-17/PVDF flexible membranes represent another representative monolithic device [101]. Bi-based CAU-17 MOF nanocrystals are grown in situ on PVDF substrates, with partial Bi sites converted into ferroelectric Bi_2WO_6 nanocrystals. The reusable integrated membrane realizes continuous dye enrichment, physical separation, and in situ piezocatalytic degradation under ambient low-frequency vibration, providing a feasible material platform for practical sewage purification.

Taken together, heterostructure construction provides a feasible route to suppress the severe piezo-generated carrier recombination that inherently limits monophasic MOF piezocatalysts. To avoid a simplistic sequential description of individual studies and to clarify the core contribution of MOF symmetry engineering, all composite systems in this section are

further classified according to the functional role of the MOF phase. Role A represents MOFs as the primary piezoelectric phase, corresponding to flexible monolithic polymer-MOF devices, including the PVA-PPy-gelatin-UiO-66-F_4 hydrogel, PDA@UiO-66-NH_2(Hf)/PVDF membrane, and BWO@CAU-17/PVDF membrane. In these systems, MOF crystals or MOF-derived ferroelectric phases dominate the piezoelectric polarization response, while the polymer matrix merely provides mechanical support and strain transmission. Thus, these systems can serve as direct experimental evidence for MOF lattice symmetry engineering. Role B defines MOFs as secondary piezoelectric contributors, interfacial modifiers, or electronically active co-catalysts, covering $BiFeO_3$/MOF, BiOCl/UiO-66, Bi_2O_2Se@Bi-MOF, C_3N_4/UiO-66, SnSe/UiO-66-NH_2, VBiTO@NU-66, and ZnO/CuO@UiO-66-NH_2 heterostructures. The improved catalytic performance of these composites primarily originates from the intrinsic piezoelectricity of inorganic counterparts ($BiFeO_3$, BiOCl, SnSe, ZnO/CuO, $Bi_4Ti_3O_{12}$), interfacial charge separation, co-catalytic effects, and enhanced adsorption capacity, rather than the lattice symmetry breaking of the MOF itself. Role C regards MOFs as porous supports and host matrices, represented by the DABT@UiO system, where the piezocatalytic activity stems from encapsulated piezoactive guest molecules instead of the MOF framework. Consequently, the catalytic performance of Role B and Role C systems cannot be treated as valid validation of bulk MOF symmetry design.

Crucially, the performance improvement of heterostructured piezocatalysts is typically driven by multiple coupled factors rather than a single symmetry effect. Variations in specific surface area, surface adsorption affinity, defect density, electrical conductivity, band structure alignment, interfacial morphology, and strain redistribution inevitably co-occur during composite construction and jointly affect catalytic outcomes. Therefore, it is unreliable to attribute performance enhancement solely to symmetry breaking without decoupling these interfering variables. Furthermore, most existing heterostructure piezocatalysis tests rely on high-power ultrasonic excitation, while systematic evaluations under low-grade ambient vibration and rigorous control experiments using centrosymmetric MOF references are still lacking. Future studies should focus on decoupling symmetry modulation effects from other structural and electronic variations to establish unambiguous and rigorous structure–activity relationships for symmetry-designed, MOF-based composite piezocatalysts.

5. Core Challenges and Progressive Research Outlook

Combined with the theoretical basis, structural advantages, multi-scale symmetry design strategies, and practical application limitations elaborated above, this chapter systematically outlines the multi-level bottlenecks restricting the industrial translation of MOFs piezocatalysis. The progressive research sequence includes fundamental dynamic mechanism characterization, low-frequency flexible lattice material design, integrated catalytic device engineering, green large-scale production, and artificial intelligence-assisted high-throughput material prescreening. Corresponding targeted innovative research directions are proposed for each bottleneck, including the emerging data-driven screening paradigm for symmetry-oriented piezocatalytic MOFs.

5.1. Ambiguity of Dynamic Strain-Polarization Fundamental Mechanisms

Current mechanistic exploration of MOFs piezocatalysis heavily depends on static ex situ post-reaction characterizations, such as steady-state PFM hysteresis loops and post-test PXRD, which cannot capture transient lattice torsion, real-time surface-bound charge density, interfacial screening ion redistribution, or dynamic band tilting under continuous mechanical oscillation. A set of unresolved characterization gaps hinders the construction of a complete mechanistic framework for hybrid MOFs lattices.

Integrated synchronous testing platforms that couple low-frequency vibration loading with time-resolved KPFM, dynamic synchrotron XAS, and in situ SHG remain largely

underexplored. Most existing in situ apparatuses are optimized for high-power ultrasonic stimulation above 40 kHz, which creates a mismatch with natural weak-vibration scenarios. A full-spectrum characterization workflow covering key piezocatalytic processes would combine multiple modules: pressure-dependent UV–Vis, Raman, and PL for bandgap and phase-transition tracking; in situ Mott–Schottky and open-circuit voltage electrochemistry for piezopotential and band-edge quantification; HAADF-STEM paired with in situ KPFM for atomic-scale polarization domain and surface screening-charge visualization; in situ EPR and FTIR for radical-intermediate identification; in situ XPS/UPS for interfacial charge-transfer and work-function measurement; and SSPFM for defect-mediated screening-charge migration analysis. Very few synchronized, multimodal testing setups have been reported that are compatible with porous, flexible MOFs.

Standardized blank experimental protocols are needed to quantitatively disentangle intrinsic piezocatalytic activity from thermal side effects originating from ultrasonic cavitation and sonochemical reactions. Appropriate control groups, including vibration-free static blanks, equal-power ultrasonic thermal blanks, and non-piezoelectric centrosymmetric MOF blanks, are required for reliable quantification. Without unified control design, correlations between strain magnitude and apparent catalytic activity extracted from published literature may contain substantial uncertainties.

In addition, widely adopted finite-element simulation models are mostly parameterized for rigid inorganic lattices and disregard the torsional degrees of freedom of flexible organic linkers within MOFs skeletons. This limitation yields imperfect predictions of screening-charge imbalance within interconnected pore spaces. Revised COMSOL simulations that incorporate linker-torsion variables are required to quantitatively map transient screening-charge distribution and dynamic band-bending gradients under microscale strain. To address the above-mentioned barriers, future fundamental research should prioritize constructing multimodal synchronized operando platforms adapted to low-frequency micro-vibration, developing revised finite-element models that account for flexible-linker deformation, and formulating universal control-experiment standards to exclude non-piezocatalytic interference and realize absolute quantification of intrinsic strain-driven catalytic performance.

5.2. Shortage of Topologically Optimized Flexible MOFs Adaptive to Natural Low-Grade Vibration

Most reported high-performing MOFs piezocatalysts are evaluated under ultrasonic conditions, whereas practical natural weak mechanical stimuli, such as ocean wave motion, low-frequency industrial vibration, and human micromovement, fall within the 5–50 Hz range. Existing topological designs for MOFs mainly concentrate on static crystal non-centrosymmetry, while dynamic lattice flexibility under micro-external-force conditions is rarely considered. Many symmetry-broken yet rigid coordination frameworks exhibit only minor linker rotation under tiny stress, resulting in insufficient charge-screening mismatch and flat interfacial band structures, which lead to activity loss under ambient-vibration conditions. Current symmetry-modulation approaches are largely confined to static crystal space-group engineering and seldom construct gradient dipole distributions along pore channels to amplify directional carrier migration upon cyclic strain. Breaking the static-symmetry-design paradigm provides a feasible route toward flexible coordination lattices with gradient dipoles suited for harvesting low-frequency vibration energy. Research efforts can be directed toward constructing flexible topological skeletons with intrinsic gradient-dipole distributions along one-dimensional pore channels via asymmetric gradient assembly of organic linkers. Soft aliphatic bridging segments can be introduced into rigid aromatic linkers to lower the energy barrier for linker torsion and enable large-amplitude reversible rotation under ultralow mechanical force. Moreover, a quantitative library of

topological descriptors correlating linker flexibility, pore anisotropy, and low-frequency piezoresponse should be established to facilitate rational prescreening of strain-responsive MOFs and reduce inefficient trial-and-error synthesis.

5.3. Lack of Scenario-Tailored Symmetry Regulation Criteria

Symmetry modification strategies applied to MOFs are generally implemented as universal schemes without targeted optimization for diverse application scenarios, giving rise to performance limitations in fields, including biomedical tumor therapy and industrial CO_2 reduction. For clinical sonodynamic tumor therapy applications, excessive piezovoltage may generate superfluous reactive oxygen species and damage normal somatic cells. Industrial CO_2 reduction imposes requirements for widened bandgaps that cannot be readily satisfied by conventional polar or chiral MOFs. Furthermore, biocompatible MOFs still lack precise Curie temperature tuning matching human physiological temperature (36–38 °C), which remains an unmet experimental target, while acid-resistant, symmetry-broken frameworks suitable for high-concentration aqueous CO_2 environments remain scarce. Establishing scenario-oriented hierarchical symmetry-engineering standards can alleviate these bottlenecks, whereby separate design frameworks are formulated for biomedical and industrial catalytic MOFs. For tumor-therapy-oriented applications, homochiral Zr/Hf-based MOFs with well-controlled mild polarity can be synthesized to avoid excessive ROS release, and their Curie temperatures can be tuned to match human physiological temperature ranges. For industrial piezocatalytic CO_2 reduction, acid-resistant, high-valent polar MOFs with widened bandgaps should be developed to satisfy multi-electron-reduction thermodynamics.

5.4. High-Cost Ligand Barrier Restricting Large-Scale Green Mass Production

State-of-the-art high-performance symmetry-engineered MOFs frequently depend on expensive fluorinated or chiral multi-amino commercial linkers, which suffer from complicated synthetic workflows and low yields. Conventional solvothermal synthesis consumes large volumes of toxic high-boiling organic solvents and fails to satisfy green-industrial-manufacturing requirements. Biomass-derived polar or chiral building blocks remain underexplored, and room-temperature aqueous one-pot synthetic methodologies for preparing non-centrosymmetric MOFs have not been well established. These factors produce high raw-material and energy costs during scale-up and hinder industrial promotion of symmetry-modified MOFs systems. Exploring biomass-derived chiral/polar ligands enables green aqueous synthesis of target MOFs. Renewable plant tannins, amino-acid by-products, and agricultural-lignin derivatives can serve as low-cost building blocks for constructing non-centrosymmetric MOFs with piezocatalytic performance comparable to materials built from commercial ligands. Room-temperature, solvent-free aqueous one-pot synthetic routes can be further developed to realize kilogram-level fabrication of UiO, ZIF, and CAU series MOFs.

5.5. AI-Assisted High-Throughput Screening of Piezocatalytic MOFs

The number of experimentally reported MOFs structures has grown to tens of thousands. Trial-and-error experimental exploration cannot efficiently identify promising piezocatalytic candidates with desirable symmetry, piezoelectric coefficient, band alignment, and chemical stability simultaneously. Artificial-intelligence-driven high-throughput virtual screening provides a feasible solution for this bottleneck.

Symmetry descriptors, mechanical response features, electronic-structure fingerprints, and synthetic feasibility metrics can be constructed as multi-dimensional input features. Target output properties cover non-centrosymmetric space-group probability, piezoelectric coefficient magnitude, Curie temperature, band-edge positions matching piezocatalytic redox reactions, and aqueous chemical durability. Machine-learning models can be trained

on existing computational and experimental datasets. Such trained models enable rapid prescreening over massive MOFs crystal databases. They narrow down material pools and only retain a small subset of high-potential candidates for subsequent DFT calculation and experimental validation.

At present, available datasets specially annotated for MOFs' piezoelectric and ferroelectric properties remain scarce. Insufficient labeled data limits the prediction accuracy of machine-learning models. Future efforts should prioritize constructing dedicated open datasets for piezocatalytic MOFs. These datasets need to integrate crystal symmetry information, mechanical deformation responses, electronic properties, and experimental stability records. Transfer-learning strategies can be adopted to mitigate data scarcity. Combined with the symmetry-centered design principles summarized in this review, AI tools will accelerate the discovery of low-cost, vibration-adapted piezocatalytic MOFs without repeated blind experimental attempts.

6. Conclusions

Fueled by the demand for harvesting low-grade mechanical energy, MOFs-based piezocatalysis has advanced rapidly. This review summarizes MOFs piezocatalysis from the perspective of crystallographic inversion symmetry engineering and establishes a three-tier multi-scale symmetry modulation framework covering atomic lattice regulation, metal-mediated dipole amplification, and heterostructure construction. Three complementary piezocatalytic mechanisms (strain-triggered band bending, space charge screening, displacement current theory) are systematically demonstrated. Reversible torsion of organic linkers within porous MOFs acts as an additional source of dipole fluctuation, which is often overlooked in conventional rigid inorganic piezoelectric models. Benefiting from reticular chemistry, MOFs can generate local lattice dipoles via artificial symmetry breaking while retaining inherent advantages, including large specific surface area, tunable active sites, favorable aqueous stability, and feasible synthetic routes. Symmetry-breaking strategies, including polar ligand grafting, metal node substitution, vacancy engineering, post-synthetic metal coordination, and heterojunction construction, have been demonstrated to enhance piezoresponse and catalytic activity in reported literature. Nevertheless, observed performance improvements are frequently entangled with concurrent variations in defects, surface area, band-edge alignment, and adsorption behavior. As highlighted throughout this review, centrosymmetric reference samples and multi-regime excitation tests are essential to decouple genuine symmetry-derived contributions from other interfering factors.

Several critical challenges still restrict the practical translation of MOFs piezocatalysis. Most high-activity MOFs piezocatalysts reported to date are tested under intense ultrasonic excitation rather than natural low-frequency ambient vibration. Powder-form catalysts commonly encounter issues including active component leaching and unsatisfactory recyclability. Synchronized operando characterization platforms tailored for flexible porous MOFs remain limited. The high cost of organic linkers and the use of toxic solvents also hinder green and scalable manufacturing. Based on the literature survey, prospective research directions include developing standardized operando characterization protocols and rigorous control experiments, designing flexible gradient-dipole MOFs suitable for weak ambient vibration, fabricating fatigue-resistant monolithic self-powered catalytic devices, and implementing AI-driven high-throughput screening built upon symmetry-annotated MOFs datasets.

It should be emphasized that these directions represent tentative forward-looking perspectives rather than established evaluation criteria. As these are exploratory concepts proposed herein, future studies may develop a cost-normalized piezocatalytic efficiency

metric integrating synthesis cost, catalyst lifetime, recyclability, and regeneration, alongside rational strategies for integrated device configuration to transform powder MOFs piezocatalysts into practical monolithic systems. A full mathematical definition and demonstrative calculation for this cost-normalized index require substantial follow-up experimental and economic data, which is beyond the scope of this review.

We anticipate that the symmetry-centered design principle summarized herein can offer theoretical guidelines for developing next-generation piezocatalytic MOFs and promote mechanical-energy-driven chemical conversion for environmental remediation and clean energy applications.

Author Contributions: Conceptualization, K.Z., S.X. H.C. and G.Z.; data curation, K.Z., A.F. and G.Z.; writing—original draft preparation, K.Z., A.F., G.Z. and B.F.; writing—review and editing, K.Z., S.X. G.Z. and B.F.; visualization, K.Z., S.X. A.C. and G.Z.; supervision, K.Z., S.X. and G.Z.; project administration, B.F.; funding acquisition, B.F. and G.Z. All authors have read and agreed to the published version of the manuscript.

Funding: This work was supported by the High-level Talents Program Startup Funds (No. 221110175) provided by Dongguan University of Technology and the High-level Talents Program (contract number 2023JC10L014) of the Department of Science and Technology of Guangdong Province, the Guangdong Basic and Applied Basic Research Foundation (Nos. 2022A1515140108; 2023A1515140049; 2023B1515120062), the Guangdong Provincial University Innovation Team Project (No. 2023KCXTD038), and Key projects of Social Science and Technology Development in Dongguan (No. 20231800936352).

Data Availability Statement: The original contributions presented in this study are included in the article. Further inquiries can be directed to the corresponding authors.

Acknowledgments: We gratefully acknowledge the support of the above-mentioned funding projects.

Conflicts of Interest: The authors declare no conflicts of interest.

Abbreviations

The following abbreviations are used in this manuscript:

MOFs	Metal–organic frameworks
BET	Brunauer–Emmett–Teller
DFT	Density Functional Theory
EPR	Electron Paramagnetic Resonance
FTIR	Fourier-Transform Infrared Spectroscopy
HAADF-STEM	High-Angle Annular Dark-Field Scanning Transmission Electron Microscopy
KPFM	Kelvin Probe Force Microscopy
MD	Molecular Dynamics
PFM	Piezoresponse Force Microscopy
PENG	Piezoelectric Nanogenerator
PL	Photoluminescence
PXRD	Powder X-Ray Diffraction
SHG	Second-Harmonic Generation
SBU	Secondary Building Unit
SSPFM	Switching Spectroscopy Piezoresponse Force Microscopy
XAS	X-Ray Absorption Spectroscopy
XPS/UPS	X-Ray Photoelectron Spectroscopy/Ultraviolet Photoelectron Spectroscopy
NLC	Negative Linear Compressibility
DART-PFM	Dual AC Resonance Tracking Piezoresponse Force Microscopy
WOR	Water Oxidation Reaction
ORR	Oxygen Reduction Reaction

References

1. Chen, L.; Jiang, Q.; Wang, X.; Lian, X.; Liang, S.; Weng, B.; Zhao, X.; Pan, X. Ti_3C_2/MoS_2 Nanocomposite Heterojunction for High-Efficiency Piezocatalytic Hydrogen Evolution. *Langmuir* **2025**, *41*, 31649–31659. [CrossRef] [PubMed]
2. Du, X.; Fu, Y.; Arandiyan, H.; Li, P.; Fan, H.; Zhu, L.; Li, H.; Zhang, L.; Ma, T. Emerging piezocatalysts: Metal–organic frameworks and their derivatives. *Nano Today* **2025**, *65*, 102841. [CrossRef]
3. Hong, K.-S.; Xu, H.; Konishi, H.; Li, X. Direct Water Splitting Through Vibrating Piezoelectric Microfibers in Water. *J. Phys. Chem. Lett.* **2010**, *1*, 997–1002. [CrossRef]
4. Zhou, L.; Meng, L.; Jia, H.; Lu, Y.; Liang, T.; Yuan, Y.; Liu, C.; Dong, Z.; Hu, L.; Guan, P.; et al. Recent Advances in Piezocatalysts for Dye Degradation. *Adv. Sustain. Syst.* **2024**, *8*, 2300652. [CrossRef]
5. Jiang, T.; Wang, Y.; Cai, C.; Nie, C.; Peng, H.; Ao, Z. Piezocatalysis for water treatment: Mechanisms, recent advances, and future prospects. *Environ. Sci. Ecotechnol.* **2025**, *23*, 100495. [CrossRef]
6. Amiri, O.; Ahmed, S.S.; Younis, K.A.; Abdullah, H.K.; Aziz, S.A. Mastering the Art: Crafting Efficient Piezo-Catalysts and Piezo-Photocatalysts for Optimal Organic Pollutant Degradation. *Chem. Afr.* **2025**, *8*, 2189–2203. [CrossRef]
7. Lu, Y.; Hao, C.; Gao, S.; Zhao, X.; An, X.; Hu, G. Piezoelectric catalysts for water pollutant remediation: Achievements, challenges, and perspectives. *Mater. Today* **2025**, *88*, 415–440. [CrossRef]
8. Gan, Y.; Li, S.; Khalid, K.; Gebreslassie, G.; Li, M.; Gebresilassie, A.B.; Liu, X.; He, L.; Lin, B. Emerging graphitic carbon nitride-based piezocatalysts for multifunctional applications: Environmental remediation, renewable energy and antibacterial technology. *Chem. Eng. J.* **2026**, *529*, 172318. [CrossRef]
9. Zhang, J.; Luan, X.; Lv, Z.; Wang, Y.; Yu, Q.; Zhong, H.; Yang, G.; Liu, H. Electron transfer driven piezocatalytic degradation of emerging contaminants: Recent advances, modification strategies, and prospects. *J. Water Process Eng.* **2025**, *75*, 108012. [CrossRef]
10. Rasheed, H.M.; Shahid, M.Z.; Ding, C.; Ruan, X.; Cui, X. Piezocatalysis for Artificial Photosynthetic Systems: Catalyst Design Strategies, Reaction Mechanism, Applications, and Future Perspectives. *Adv. Sustain. Syst.* **2026**, *10*, e01215. [CrossRef]
11. He, J.; Zhang, M.; Duan, X.; Zhu, M. In Situ Evidence Unveiling the Debate of Mechanism for Piezo-Catalysis. *ACS Catal.* **2026**, *16*, 13909–13921. [CrossRef]
12. Xu, X.; Wang, Y.; Cheng, W.; Zhai, H.; Xiao, L.; Qin, L.; Chen, D. Recent advances in piezocatalytic hydrogen production and prospects. *Surf. Interfaces* **2024**, *54*, 105245. [CrossRef]
13. Wang, Y.; Chen, Y.; Cheng, J.; Zhuang, J.; Han, F.; An, Q.; Bai, R. Acid-engineering combined heterojunction formation for high efficient piezo-catalytic FeCo-LDH@ZnO. *Nano Energy* **2025**, *144*, 111333. [CrossRef]
14. Zhang, Y.; Feng, K.; Song, M.; Xiang, S.; Zhao, Y.; Gong, H.; Ni, F.; Dietrich, F.; Fulanović, L.; Zhuo, F.; et al. Dislocation-engineered piezocatalytic water splitting in single-crystal $BaTiO_3$. *Energy Environ. Sci.* **2025**, *18*, 602–612. [CrossRef]
15. Chen, N.; Han, J.; He, X.; Shao, J.; Li, N.; Chen, D.; Lu, J. Hydrophilic PVDF membrane doped with Ti_3C_2 for piezocatalytic purification of water flow. *J. Environ. Chem. Eng.* **2025**, *13*, 117829. [CrossRef]
16. Kumar, S.; Sharma, S.K.; Tripathi, H.; Vaish, R.; Chauhan, V.S.; Singh, G. Flexible and electroactive phase-rich BZT–BST/PVDF composite films for efficient piezocatalysis. *Mater. Sci. Semicond. Process.* **2026**, *212*, 110783. [CrossRef]
17. Silakhao, P.; Rattanakam, R.; Jettanasen, J. Dual-functional $BiFeO_3$-based PVDF/CNF composite films for adsorption-assisted piezocatalytic degradation of methylene blue. *Surf. Interfaces* **2026**, *94*, 109651. [CrossRef]
18. Liu, J.; Liao, W.; Li, D.; Zhang, Y.; Li, X.; Zhang, Y.; Ma, Z.; Liu, Z.; Xu, L.; Li, H. Highly self-polarized PVDF-based nanocomposites achieved via water mediated polarization for advanced piezocatalysis. *Ceram. Int.* **2026**, *52*, 16878–16890. [CrossRef]
19. Mohammadi, Z.; Rahman Setayesh, S. Bi-internal electric field/Schottky barrier integrated in flexible $Ag_2/BiFe_{0.9}Mn_{0.1}O_3$@PVDF composite membrane to promote piezocatalytic degradation of tetracycline-hydrochloride antibiotic. *Chem. Eng. J.* **2026**, *530*, 173829. [CrossRef]
20. Xie, B.; Gao, W.; Liu, Z.; Guo, K.; Wang, Q.; Jiang, S.; Bowen, C.; Luo, H.; Li, T. Superior Piezocatalytic Activity and Environmental Adaptability in Micro-Nano-Engineered $BaTiO_3$/PVDF@Ag Composite Structure. *Adv. Funct. Mater.* **2026**, *36*, e77213. [CrossRef]
21. Mussa, N.-S.; Toshtay, K.; Dumeignil, F. Recent developments in the field of MOF-based catalytic systems: A review. *Appl. Catal. A Gen.* **2025**, *708*, 120555. [CrossRef]
22. Zulfiqar, A.; Miao, B.; Khan, F.; Ali, N.; Ahmed, S.; Rehman, W.; Asad, M.; Nawaz, M.A.; Mir, I.A.; Rasheed, L. Metal–Organic Framework (MOF)-Based Catalysts for Sustainable Energy Technologies: A Review. *Langmuir* **2025**, *41*, 24049–24077. [CrossRef] [PubMed]
23. Niu, Y.; Wang, Y.; Zhang, H. MOF in catalysis, sensing and energy storage applications. *Nano Energy* **2026**, *147*, 111598. [CrossRef]
24. Kumar, N.; Patial, B.; Navdeep; Gupta, R.; Bansal, A. From framework to function: MOF-derived nanoparticles in photocatalysis, electrocatalysis, adsorption, and energy storage. *Coord. Chem. Rev.* **2026**, *550*, 217391. [CrossRef]
25. Rehman, A.U.; Asghar, M.; Rauf, A.; Najam, T.; Shaaban, I.A.; Shah, S.S.A.; Nazir, M.A. MOF/Graphene interfaces in catalytic water splitting: Recent breakthroughs and future outlook. *Fuel* **2026**, *405*, 136800. [CrossRef]

26. Qureshi, W.A.; Haider, S.N.-U.-Z.; Qaiser, M.A.; Khan, S.; Wang, W.; Ali, R.N.; Ali, A.; Naveed, A.; Abdurahman, M.H.; Khan, M.U.; et al. Breakthrough in plasmonic enhanced MOFs: Design, synthesis, and catalytic mechanisms for various photocatalytic applications. *Environ. Res.* **2025**, *277*, 121257. [CrossRef] [PubMed]
27. Javed, S.; Ullah, S.; Hasanov, R.; Asghar, M.; Shaaban, I.A.; Rahman, M.M.; Akkinepally, B.; Shah, S.S.A.; Nazir, M.A. MOF@GO composites for effective hydrogen production via photocatalytic water splitting. *J. Alloys Compd.* **2025**, *1048*, 185283. [CrossRef]
28. Keshta, B.E.; Abdalla, S.; Tesnim, D.; Abou El-Reash, Y.G.; Al-Farraj, E.S.; Shaban, M.M.; El-Harairy, A.; El-Saeed, H.M.; El-Harairy, A.; Shaban, E.A.; et al. MOF-based catalysts for sustainable biodiesel production: Classification, performance, and advances from 2020 to 2025. *RSC Adv.* **2025**, *15*, 48692–48726. [CrossRef] [PubMed]
29. Abdurahman, M.H.; Rhimi, B.; El-Khodary, S.A.; Abdullah, A.Z.; Okoye, P.; Asghar, M.R.; Liu, Q. Structural tailoring of metal–organic frameworks for photocatalytic degradation of contaminant emergence concern: Recent advances and perspectives. *Sep. Purif. Technol.* **2025**, *376*, 134016. [CrossRef]
30. Afreen, N.; Ahmad, N.; Kumar, G.; Anwer, A.H.; Benamor, A.; Coulon, F.; Ahmad, N. Porphyrin-Based Metal–Organic Frameworks as Sustainable Photocatalysts for Micropollutant Degradation: A Critical Review on Structure, Mechanism and Future Perspectives. *ACS ES&T Water* **2025**, *5*, 2028–2040. [CrossRef]
31. Sivasurya, E.; Atchudan, R.; Mohamed, M.G.; Thangamani, A.; Rajendran, S.; Jalil, A.; Kalambate, P.K.; Manoj, D.; Kuo, S.-W. Electrocatalytic conversion of CO_2 into selective carbonaceous fuels using metal-organic frameworks: An overview of recent progress and perspectives. *Mater. Today Chem.* **2025**, *44*, 102538. [CrossRef]
32. Zou, X.; Shi, Q.; Cheng, M.; Huang, D.; Zhang, G.; Wang, W.; Wang, G.; Liu, H.; Chen, Y.; Chen, A.; et al. Metal–Organic Framework-Based Materials for Photocatalytic Hydrogen Peroxide Production: Insights into Mechanism, Modification Strategies, and Environmental Applications. *Adv. Energy Mater.* **2025**, *15*, 2501424. [CrossRef]
33. Anadebe, V.C.; Thakur, A.; Verma, C.; Mamba, B.B.; Alfantazi, A.; Ebenso, E.E.; Barik, R.C. Unveiling cutting-edge progress in coordination chemistry of the metal-organic frameworks (MOFs) and their composites: Fundamentals, synthesis strategies, electrochemical and environmental applications. *J. Ind. Eng. Chem.* **2025**, *148*, 247–299. [CrossRef]
34. Mehmood, R.A.; Aslam, A.A.; Iqbal, M.J.; Sajid, A.H.; Hamza, A.; Tahira, H.F.; Islam, I.U.; Yabalak, E. A review on hydrogen production using decorated metal-organic frameworks by electrocatalytic and photocatalytic water splitting. *Fuel* **2025**, *387*, 134416. [CrossRef]
35. Silerio-Vázquez, F.d.J.; Hosseini-Bandegharaei, A.; Abdikalykov, R.; Baigenzhenov, O.; Kakavandi, B.; Robledo-Peralta, A. Recycled PET-derived MOF for photocatalytic degradation of emerging pollutants: Recent progress and critical considerations. *Environ. Res.* **2026**, *288*, 123231. [CrossRef] [PubMed]
36. Fu, D.-W.; Zhang, W.; Xiong, R.-G. The first metal–organic framework (MOF) of Imazethapyr and its SHG, piezoelectric and ferroelectric properties. *Dalton Trans.* **2008**, *37*, 3946–3948. [CrossRef] [PubMed]
37. Wang, C.; Zhang, T.; Lin, W. Rational Synthesis of Noncentrosymmetric Metal–Organic Frameworks for Second-Order Nonlinear Optics. *Chem. Rev.* **2011**, *112*, 1084–1104. [CrossRef] [PubMed]
38. Sun, Y.; Gao, J.; Cheng, Y.; Zhang, Y.-W.; Zeng, K. Design of the Hybrid Metal–Organic Frameworks as Potential Supramolecular Piezo-/Ferroelectrics. *J. Phys. Chem. C* **2019**, *123*, 3122–3129. [CrossRef]
39. Zhang, X.; Guo, K.; Peng, L.; Wu, J.; Zhang, F.; Zhu, W.; Fu, Y. Degradation of Dye Wastewater over NH_2-UiO-66: Piezoelectrically Induced Mechano-Catalytic Effect. *J. Inorg. Mater.* **2020**, *35*, 1023–1028. [CrossRef]
40. Zhang, C.; Lei, D.; Xie, C.; Hang, X.; He, C.; Jiang, H.-L. Piezo-Photocatalysis over Metal–Organic Frameworks: Promoting Photocatalytic Activity by Piezoelectric Effect. *Adv. Mater.* **2021**, *33*, 2106308. [CrossRef] [PubMed]
41. Fisher, T.M.; Mohlala, T.; Sebokolodi, T.I.; Sipuka, D.S.; Jayeola, K.D.; Masukume, M.; Mabuba, N.; Garcia-Segura, S.; Arotiba, O.A. Metal-organic framework (MOF) catalysts for piezocatalytic water treatment: Progress, limitations, and future prospects. *J. Sci. Adv. Mater. Devices* **2026**, *11*, 101211. [CrossRef]
42. Jin, J.; Liu, Y.; Gao, H.; Zhang, S.; Yan, X.; Cui, H.; Mukaddas, A.; Ji, T.; Guan, P.; Weng, Y.; et al. MOF etching and hydrogel confinement: A dual strategy for high-performance MOF-based synergistic piezo-photocatalysis. *Sep. Purif. Technol.* **2026**, *387*, 136715. [CrossRef]
43. Wang, Y.; Su, P.; Lin, Z.; Li, X.; Chen, K.; Ye, T.; Li, Y.; Zou, Y.; Wang, W. A Tribo/Piezoelectric Nanogenerator Based on Bio-MOFs for Energy Harvesting and Antibacterial Wearable Device. *Adv. Mater.* **2025**, *37*, 2418207. [CrossRef] [PubMed]
44. Shaukat, R.A.; Saqib, Q.M.; Kim, J.; Song, H.; Khan, M.U.; Chougale, M.Y.; Bae, J.; Choi, M.J. Ultra-robust tribo- and piezo-electric nanogenerator based on metal organic frameworks (MOF-5) with high environmental stability. *Nano Energy* **2022**, *96*, 107128. [CrossRef]
45. Rao, K.K.; Sarkar, D.; Ravipati, M.; Badhulika, S. Rapid-response Self-Powered piezoelectric pressure sensor based on Zn-MOF nanorod/Zr-MOF-PVDF nanofiber for bio-mechanical sensing and machine learning -enabled Smart glove object classification. *Mater. Sci. Eng. B* **2026**, *330*, 119553. [CrossRef]
46. You, H.; Wu, Z.; Zhang, L.; Ying, Y.; Liu, Y.; Fei, L.; Chen, X.; Jia, Y.; Wang, Y.; Wang, F.; et al. Harvesting the Vibration Energy of $BiFeO_3$ Nanosheets for Hydrogen Evolution. *Angew. Chem. Int. Ed.* **2019**, *58*, 11779–11784. [CrossRef] [PubMed]

47. Ma, J.; Jing, S.; Wang, Y.; Liu, X.; Gan, L.-Y.; Wang, C.; Dai, J.-Y.; Han, X.; Zhou, X. Piezo-Electrocatalysis for CO_2 Reduction Driven by Vibration. *Adv. Energy Mater.* **2022**, *12*, 2200253. [CrossRef]
48. Ren, Z.; Chen, F.; Zhao, Q.; Zhao, G.; Li, H.; Sun, W.; Huang, H.; Ma, T. Efficient CO_2 reduction to reveal the piezocatalytic mechanism: From displacement current to active sites. *Appl. Catal. B Environ.* **2023**, *320*, 122007. [CrossRef]
49. Mula, S.; Huang, C.; Grozema, F.; van der Veen, M.A. Computational screening of piezoelectric constants in metal–organic frameworks: Design principles and ferroelectric-like bond modulation. *J. Mater. Chem. A* **2026**, *14*, 14311–14323. [CrossRef] [PubMed]
50. Mula, S.; Donà, L.; Civalleri, B.; van der Veen, M.A. Structure–Property Relationship of Piezoelectric Properties in Zeolitic Imidazolate Frameworks: A Computational Study. *ACS Appl. Mater. Interfaces* **2022**, *14*, 50803–50814. [CrossRef] [PubMed]
51. Kitou, S.; Ishikawa, H.; Tokunaga, Y.; Ueno, M.; Sawa, H.; Nakamura, Y.; Kinoshita, Y.; Miyamoto, T.; Okamoto, H.; Kindo, K.; et al. Piezoelectric Transition in a Nonpyroelectric Gyroidal Metal–Organic Framework. *J. Am. Chem. Soc.* **2025**, *147*, 13642–13648. [CrossRef] [PubMed]
52. Yang, T.-Y.; Li, Z.-G.; Lang, F.; Dong, X.-H.; Zhao, C.; Zhang, G.-L.; Li, Z.-Y.; Chang, Z.; Feng, R.; Li, W.; et al. Large Piezoelectricity in a Dynamic Metal–Organic Framework With Negative Linear Compressibility. *J. Am. Chem. Soc.* **2025**, *147*, 41988–41994. [CrossRef] [PubMed]
53. Asadi, K.; van der Veen, M.A. Ferroelectricity in Metal–Organic Frameworks: Characterization and Mechanisms. *Eur. J. Inorg. Chem.* **2016**, *2016*, 4332–4344. [CrossRef]
54. Zhang, W.; Xiong, R.-G. Ferroelectric Metal–Organic Frameworks. *Chem. Rev.* **2011**, *112*, 1163–1195. [CrossRef] [PubMed]
55. Yang, P.; He, X.; Li, M.-X.; Ye, Q.; Ge, J.-Z.; Wang, Z.-X.; Zhu, S.-R.; Shao, M.; Cai, H.-L. The first homochiral coordination polymer with temperature-independent piezoelectric and dielectric properties. *J. Mater. Chem.* **2012**, *22*, 2398–2400. [CrossRef]
56. Xue, F.; Cao, J.; Li, X.; Feng, J.; Tao, M.; Xue, B. Continuous-flow synthesis of MIL-53(Cr) with a polar linker: Probing the nanoscale piezoelectric effect. *J. Mater. Chem. C* **2021**, *9*, 7568–7574. [CrossRef]
57. Sun, Y.; Hu, Z.; Zhao, D.; Zeng, K. Probing nanoscale functionalities of metal–organic framework nanocrystals. *Nanoscale* **2017**, *9*, 12163–12169. [CrossRef] [PubMed]
58. Roy, K.; Jana, S.; Ghosh, S.K.; Mahanty, B.; Mallick, Z.; Sarkar, S.; Sinha, C.; Mandal, D. Three-Dimensional MOF-Assisted Self-Polarized Ferroelectret: An Effective Autopowered Remote Healthcare Monitoring Approach. *Langmuir* **2020**, *36*, 11477–11489. [CrossRef] [PubMed]
59. Panda, S.N.; Pradhan, P.; Nath, S.; Mohapatra, J.; Patra, B.K.; Biswal, B.P. Inducing piezoelectric behavior in a copper iodide cubane cluster-based metal–organic framework via linker engineering. *Chem. Commun.* **2025**, *61*, 2536–2539. [CrossRef] [PubMed]
60. Kabiraj, A.; Kumar, M.; Mahapatra, S. High-throughput discovery of high Curie point two-dimensional ferromagnetic materials. *NPJ Comput. Mater.* **2020**, *6*, 35. [CrossRef]
61. Lv, H.; Li, X.; Wu, D.; Liu, Y.; Li, X.; Wu, X.; Yang, J. Enhanced Curie Temperature of Two-Dimensional Cr(II) Aromatic Heterocyclic Metal–Organic Framework Magnets via Strengthened Orbital Hybridization. *Nano Lett.* **2022**, *22*, 1573–1579. [CrossRef] [PubMed]
62. Loiseau, T.; Serre, C.; Huguenard, C.; Fink, G.; Taulelle, F.; Henry, M.; Bataille, T.; Férey, G. A Rationale for the Large Breathing of the Porous Aluminum Terephthalate (MIL-53) Upon Hydration. *Chem.—A Eur. J.* **2004**, *10*, 1373–1382. [CrossRef] [PubMed]
63. Cavka, J.H.; Jakobsen, S.; Olsbye, U.; Guillou, N.; Lamberti, C.; Bordiga, S.; Lillerud, K.P. A New Zirconium Inorganic Building Brick Forming Metal Organic Frameworks with Exceptional Stability. *J. Am. Chem. Soc.* **2008**, *130*, 13850–13851. [CrossRef] [PubMed]
64. Horcajada, P.; Surblé, S.; Serre, C.; Hong, D.-Y.; Seo, Y.-K.; Chang, J.-S.; Grenèche, J.-M.; Margiolaki, I.; Férey, G. Synthesis and catalytic properties of MIL-100(Fe), an iron(iii) carboxylate with large pores. *Chem. Commun.* **2007**, *43*, 2820–2822. [CrossRef] [PubMed]
65. Park, K.S.; Ni, Z.; Côté, A.P.; Choi, J.Y.; Huang, R.; Uribe-Romo, F.J.; Chae, H.K.; O'Keeffe, M.; Yaghi, O.M. Exceptional chemical and thermal stability of zeolitic imidazolate frameworks. *Proc. Natl. Acad. Sci. USA* **2006**, *103*, 10186–10191. [CrossRef] [PubMed]
66. Kandiah, M.; Nilsen, M.H.; Usseglio, S.; Jakobsen, S.; Olsbye, U.; Tilset, M.; Larabi, C.; Quadrelli, E.A.; Bonino, F.; Lillerud, K.P. Synthesis and Stability of Tagged UiO-66 Zr-MOFs. *Chem. Mater.* **2010**, *22*, 6632–6640. [CrossRef]
67. Yang, L.; Qiu, T.; Shen, M.; He, H.; Huang, H. Metal-organic frameworks $Co_3[Co(CN)_6]_2$: A promising candidate for dramatically reinforcing the piezoelectric activity of PVDF. *Compos. Sci. Technol.* **2020**, *196*, 108232. [CrossRef]
68. Akeremale, O.K.; Ore, O.T.; Bayode, A.A.; Badamasi, H.; Adedeji Olusola, J.; Durodola, S.S. Synthesis, characterization, and activation of metal organic frameworks (MOFs) for the removal of emerging organic contaminants through the adsorption-oriented process: A review. *Results Chem.* **2023**, *5*, 100866. [CrossRef]
69. Li, X.-J.; Wang, F.; Dong, Y.; Ho, S.-H.; Wang, C.-C. Quasi-MOFs in water treatment: Synthesis, characterization, and applications. *Environ. Sci. Ecotechnology* **2026**, *29*, 100650. [CrossRef] [PubMed]
70. Achenbach, B.; Yurdusen, A.; Stock, N.; Maurin, G.; Serre, C. Synthetic Aspects and Characterization Needs in MOF Chemistry—From Discovery to Applications. *Adv. Mater.* **2025**, *37*, 2411359. [CrossRef] [PubMed]

71. Li, H.; Jiao, H.; Zhang, X.; Fan, Z.; Wang, Y.; Wang, H.; Pei, W.; Fan, X.; Zhang, J.; Bu, X.-H. Functional Groups Induced Microenvironment Regulation of Pt Catalytic Sites in MOF/COF Heterojunction for Enhanced Photocatalytic Hydrogen Evolution. *Adv. Funct. Mater.* **2026**, *36*, e75908. [CrossRef]
72. Wang, X.; Ma, Y.; Jiang, J.; Li, M.; Li, T.; Li, C.; Dong, S. Cl-based functional group modification MIL-53(Fe) as efficient photocatalysts for degradation of tetracycline hydrochloride. *J. Hazard. Mater.* **2022**, *434*, 128864. [CrossRef] [PubMed]
73. Liu, M.; Tian, Y.; Liu, Z. Effective Enhancement of the Ferroelectric Performance of Polar Co-Gallate MOF by Doping M^{2+} Ions (M = Mg, Mn, Ni) into Framework Nodes. *Inorg. Chem.* **2023**, *62*, 7024–7031. [CrossRef] [PubMed]
74. Liu, M.; Tian, Y.; Liu, Z. A Strategy to Enhance the Ferroelectric Behavior of MOF-802(Hf) via Doping Zr4+ Ions. *Inorg. Chem.* **2023**, *62*, 8285–8292. [CrossRef] [PubMed]
75. Du, W.; Xu, X.; Yang, R.; Qiao, Y.; Yu, Y.; Tao, L.; Hu, J.; Huang, Y.; Zhu, M. Amino-enhanced MIL-101(Fe) piezocatalysis for in-situ hydrogen peroxide generation and selective production of $^1O_2$ for organic pollutants degradation. *Chem. Eng. J.* **2025**, *519*, 164967. [CrossRef]
76. Ding, R.; Liu, Q.; Zheng, L. Piezoelectric Metal-Organic Frameworks Mediated Mechanoredox Borylation and Arylation Reactions by Ball Milling. *Chem.—A Eur. J.* **2023**, *29*, e202203792. [CrossRef] [PubMed]
77. Guo, Z.; Li, N.; Zuo, S.; Qiang, C.; Zhan, W.; Li, Z.; Ma, J. Construction of a novel metal–organic framework adenine-UiO-66 piezocatalyst for efficient diclofenac removal. *Sep. Purif. Technol.* **2022**, *289*, 120743. [CrossRef]
78. Ding, Y.; Zhu, R.; Zhou, J.; Xu, W.; Pan, F.; Yang, D.; He, J.; Wu, Z.; Li, Y.; Xie, C.; et al. Enhanced piezoelectric catalytic degradation of tetracycline by -NO_2-functionalized MIL-101(Fe) via modulating electron polarization. *J. Environ. Chem. Eng.* **2026**, *14*, 122946. [CrossRef]
79. Zhao, S.; Liu, M.; Zhang, Y.; Zhao, Z.; Zhang, Q.; Mu, Z.; Long, Y.; Jiang, Y.; Liu, Y.; Zhang, J.; et al. Harvesting mechanical energy for hydrogen generation by piezoelectric metal–organic frameworks. *Mater. Horiz.* **2022**, *9*, 1978–1983. [CrossRef] [PubMed]
80. Zhao, S.; Liu, Y.; Li, Y.; Yang, X.; Huang, J.; Wang, J.; Tao, C.-a. Mechanical degradation of organic pollutants by piezoelectric metal-organic frameworks. *Mater. Today Sustain.* **2023**, *24*, 100597. [CrossRef]
81. Yuan, W.; Yao, H.; Zhang, J.; Sunarso, J.; Zhang, Y.; Li, F. Piezocatalytic Generation of Hydrogen Peroxide Over UiO-66: Effect of Metal Centers Modulation. *Asia-Pac. J. Chem. Eng.* **2025**, *20*, e70013. [CrossRef]
82. Li, Y.; Li, Z.; Lin, X.; Lv, H.; Zhu, M. Modulating the metal center in MIL-101 for the piezoelectric catalytic synthesis of hydrogen peroxide. *Chem. Commun.* **2023**, *59*, 5749–5752. [CrossRef] [PubMed]
83. Dong, S.; Wang, L.; Lou, W.; Shi, Y.; Cao, Z.; Zhang, Y.; Sun, J. Bi-MOFs with two different morphologies promoting degradation of organic dye under simultaneous photo-irradiation and ultrasound vibration treatment. *Ultrason. Sonochemistry* **2022**, *91*, 106223. [CrossRef] [PubMed]
84. Wang, B.; Sun, Z.; Chen, J.; Ye, J.; Kumar, A.; Ren, P.; Zhang, G.; Zhang, J. Optimizing the piezocatalytic hydrogen production activity of metal–organic frameworks through precise defect engineering. *J. Mater. Chem. A* **2026**, *14*, 18291–18306. [CrossRef]
85. Wang, Y.; Zhang, N.; Wang, R.; He, Y.; Zhou, H.; Li, X.; Gao, G.; Sun, H.; Liu, X. Bimetallic UiO-66-NH_2(Zr–Hf) synergistic photocatalytic and piezoelectric effects for the degradation of rhodamine B. *Dalton Trans.* **2023**, *52*, 10079–10088. [CrossRef] [PubMed]
86. Liu, T.; Liu, Z.; Lv, G.; Guo, L.; Liu, M.; Guo, J.; Wang, G.; Zhang, Z.; Liu, Y.; Wang, L.; et al. Efficient Dual-Path Piezosynthesis of Hydrogen Peroxide by Breaking Symmetry of UiO-66. *Adv. Funct. Mater.* **2026**, *36*, e74769. [CrossRef]
87. Hu, H.; Li, X.; Zhang, K.; Yan, G.; Kong, W.; Qin, A.; Ma, Y.; Li, A.; Wang, K.; Huang, H.; et al. Dual Modification of Metal–Organic Frameworks for Exceptional High Piezo-Photocatalytic Hydrogen Production. *Adv. Mater.* **2025**, *37*, 2419023. [CrossRef] [PubMed]
88. Zhang, K.; Feng, A.; Xu, S.; Chen, H.; Ou, C.; Wu, Q.; Yu, H.; Fang, B.; Zhong, G. Transition Metal Ions Anchored to Metal Organic Frameworks for Exceptionally High Piezocatalytic Hydrogen Production. *ACS Sustain. Chem. Eng.* **2026**, *14*, 8670–8684. [CrossRef]
89. Hao, C.; Guan, X.; Wu, Y.; Zhu, L.; Mai, Y.; Frauenheim, T.; Fu, Z.; Lu, Y.; Wang, S.; Liu, H.; et al. Activating a Metallization Switch for Record Hydrogen Evolution in Single-Atom Modified Polar MOF Piezocatalysts. *Adv. Mater.* **2026**, *38*, e23489. [CrossRef] [PubMed]
90. Che, C.; Li, R.; Jia, T.; Wang, W.; Zeng, D.; Qin, X.; Xu, S.; Jiang, B.; Wang, W.; Yang, H.; et al. Selective Oxidation of Methane by Piezoelectric Catalysis Under Mild Conditions. *ChemCatChem* **2025**, *17*, e202402105. [CrossRef]
91. Fisher, T.M.; Mohlala, T.; Jayeola, K.D.; Sebokolodi, T.I.; Sipuka, D.S.; Mabuba, N.; Garcia-Segura, S.; Arotiba, O.A. MOF-bismuth ferrite semiconductor composites: Electrochemical insights for piezocatalytic and photocatalytic water treatment applications. *Catal. Today* **2026**, *476*, 115900. [CrossRef]
92. Qiu, X.; Xie, J.; Ning, X.; Cao, Y.; Lu, Z.; Hu, J.; Hao, A. Enhancing the piezocatalytic performance for H_2 evolution by constructing BiOCl/UiO-66 heterostructure. *Appl. Surf. Sci.* **2024**, *670*, 160694. [CrossRef]
93. Xu, K.; Liu, X.; Zhang, X.; Shao, W.; Rehman, A.U.; Zhang, Y.; Zhang, L.; Zhang, J.; Liu, Y.; Sun, H.; et al. Enhanced piezocatalytic H_2O_2 production from water and air over Bi-MOF coated Bi_2O_2Se nanosheets. *Mol. Catal.* **2025**, *587*, 115485. [CrossRef]

94. Yang, J.; Li, Z.; Chen, H.; Leng, J.; Gong, L.; Zhu, M. Interfacial electric field in Zr-MOF-grafted carbon nitride to boost H_2O_2 piezo-synthesis under ambient conditions. *Chem. Commun.* **2025**, *61*, 16568–16571. [CrossRef] [PubMed]
95. Liu, H.; Li, S.; Liu, M.; Sun, P.; Zhang, X.; Zhang, L.; Zhang, Y.; Contreras-Jiménez, G.; Potier, J.; Sun, Z.; et al. Mechanically driven selective organic oxidation using MOF-coated piezoelectric SnSe nanosheets. *Nano Energy* **2025**, *142*, 111241. [CrossRef]
96. Qian, Y.; Tian, W.; Han, J.; Li, N.; Chen, D.; Xu, Q.; Li, H.; Lu, J. Bismuth vacancies-enriched $Bi_4Ti_3O_{12}$ nanosheets coated with UiO-66-NH_2 for adsorption-combined piezocatalytic oxidation of HCHO. *Sep. Purif. Technol.* **2023**, *322*, 124379. [CrossRef]
97. Huang, M.; Li, W.; Li, Y.; Tang, J.; Xu, X. Turning on and off metal-organic frameworks for the formation of novel core-shell heterojunction catalysts and the controlled piezocatalysis. *Chem. Eng. J.* **2025**, *524*, 169378. [CrossRef]
98. Guan, Y.; Zeng, X.; Liu, S.; Yao, K.; Hu, Z.; Xiao, L.; Fang, Z.; Yang, Y.; Liu, H. Construction of a Ternary ZnO/CuO@UiO-66-NH_2 Heterojunction for Efficient Piezo-Electric Degradation of Rhodamine B. *Top. Catal.* **2025**. [CrossRef]
99. Kumari, R.; Sarkar, D.; Tripathi, C.S.P.; Badhulika, S. Vortex-induced energy-efficient heavy metal reduction and dyes degradation using a piezoelectric PVA-PPy-Gelatin-UiO-66 (Zr)-F_4 MOF hybrid hydrogel. *Mater. Res. Bull.* **2026**, *204*, 114324. [CrossRef]
100. Yang, Z.; Tian, M.; Chen, C.; Zhao, Z.; Zhao, L.; Xu, J.; Yu, W.; Lin, H.; Shen, L. Interfacial energy homogenization enables β-phase transition and high piezoactivity in MOF/PVDF membrane for sustainable pollutant degradation. *Chem. Eng. J.* **2026**, *545*, 179319. [CrossRef]
101. Kang, Z.; Bao, D.; Chen, M.; Qin, N.; Wu, J. Self-cleaning MOF integrated membrane embedded with piezocatalytic Bi_2WO_6 nanocrystals for synergistic wastewater purification and dyes removal. *Process Saf. Environ. Prot.* **2024**, *181*, 312–323. [CrossRef]
102. Yu, Z.; Wang, D.; Zheng, T.; Zavabeti, A.; Wang, Y.; Wu, C.; Yang, J.; Guo, Y.; Webley, P.A.; Li, G.K. Structural engineering through modulator incorporation in UiO-66-NH_2 metal–organic frameworks for piezoresponse regulation. *J. Mater. Chem. A* **2025**, *13*, 8368–8374. [CrossRef]